The Astronomical Journal, 171:321 (22pp), 2026 May https://doi.org/10.3847/1538-3881/ae5b78

The Transit Timing and Transmission Spectrum of Hot Jupiter WASP-43 b from a Decade of Multiband Transit follow-up Observations

Napaporn A-thano[1], Supachai Awiphan[1], Eamonn Kerins[2], Akshay Priyadarshi[2], Iain McDonald[2,3], Ing-Guey Jiang[4], Yogesh C. Joshi[5], Fan Yang[6], Ida Janiak[2], Patcharawee Munsaket[7], Yasir Abdul Qadir[8], Ronnakrit Rattanamala[9], Orarik Tasuya[1,10], Ekburus Boonsoy[7,11], Nuanwan Sanguansak[7,12], Rattiyakorn Rattanasai[1,10], Thammasorn Padjaroen[10], Siramas Komonjinda[10], Sawatkamol Pichadee[1], Ananpol Sudsap[1], Smanchan Chandaiam[1], Boonyarit Choonhakit[1], Suwanit Wutsang[1], and Vik S Dhillon[13,14]

[1] National Astronomical Research Institute of Thailand, 260 Moo 4, Donkaew, Mae Rim, Chiang Mai, 50180, Thailand; napaporn@narit.or.th, supachai@narit.or.th
[2] Jodrell Bank Centre for Astrophysics, University of Manchester, Oxford Road, Manchester, M13 9PL, UK
[3] Department of Physical Sciences, The Open University, Walton Hall, Milton Keynes, MK7 6AA, UK
[4] Department of Physics and Institute of Astronomy, National Tsing-Hua University, Hsinchu 30013, Taiwan
[5] Aryabhatta Research Institute of Observational Sciences (ARIES), Manora Peak, Nainital 263001, India
[6] Département d'Astrophysique/AIM, CEA/IRFU, CNRS/INSU, Univ. Paris-Saclay, Univ. de Paris, 91191, Gif-sur-Yvette, France
[7] School of Physics, Institute of Science, Suranaree University of Technology, 111 University Avenue, Suranaree, Nakhon Ratchasima 30000, Thailand
[8] Department of Physics and Astronomy, FI-20014 University of Turku, Finland
[9] Department of Physics and General Science, Faculty of Science and Technology, Nakhon Ratchasima Rajabhat University, Nakhon Ratchasima, 30000, Thailand
[10] Department of Physics and Materials Science, Faculty of Science, Chiang Mai University, Chiang Mai, 50200, Thailand
[11] Center of Excellence for Entrepreneurship, Suranaree University of Technology, Nakhon Ratchasima, 30000, Thailand
[12] National Science and Technology Development Agency, Thailand Science Park, Pathum Thani 12120, Thailand
[13] Department of Physics and Astronomy, University of Sheffield, Sheffield, S3 7RH, UK
[14] Instituto de Astrofísica de Canarias, E-38205 La Laguna, Tenerife, Spain
Received 2025 March 13; revised 2026 March 2; accepted 2026 April 1; published 2026 May 5

Abstract

We present a new set of 35 transit light curves of the hot Jupiter WASP-43 b, obtained through the SPEARNET network. These datasets were analyzed together with previously published ground-based observations, as well as space-based data from TESS, Hubble Space Telescope (HST), and JWST, to refine the planetary parameters of WASP-43 b. A total of 188 midtransit times, measured with `TransitFit`, were analyzed for potential timing variations. The transit timing variations do not show any significant evidence of orbital decay. Atmospheric retrievals using HST/WFC3 G141 transmission spectra suggest that higher-temperature solutions are associated with higher water abundances. However, when these data are combined with observations from ground-based telescopes, TESS, and JWST, the increased modeling complexity across the broad wavelength baseline presents significant challenges for atmospheric characterization. These results highlight that high-precision, multi-instrument datasets will be necessary to break existing degeneracies in the atmospheric modeling of this target in the future.

Unified Astronomy Thesaurus concepts: Exoplanet astronomy (486); Transit photometry (1709); Timing variation methods (1703); Exoplanet atmospheres (487)

Materials only available in the online version of record: machine-readable tables

1. Introduction

WASP-43b, a hot Jupiter with an ultrashort orbital period of 0.81 days around the young K7 dwarf star WASP-43 ($V = 12.4$), was initially discovered by the Wide-Angle Search for Planets (WASP) survey (C. Hellier et al. 2011). WASP-43 b is a prime candidate for investigating transit timing variations (TTVs), due to its short orbital period. The first TTV study was conducted by M. Gillon et al. (2012), who found that the transit timing residuals diagram ($O - C$, observed minus computed) indicated that the midtransit times were consistent with a linear ephemeris. G. Maciejewski et al. (2013) found that the orbital period of WASP-43 b was shorter by 0.13 s compared to the value reported by M. Gillon et al. (2012). In 2014, J. Blecic et al. (2014) and F. Murgas et al. (2014) applied a quadratic fitting model to the transit timing data and reported a potential orbital period decay. However, studies by G. Chen et al. (2014) and D. Ricci et al. (2015) noted that there was no significant evidence for orbital decay in WASP-43 b. In 2016, I.-G. Jiang et al. (2016) presented a possible orbital decay in WASP-43b with a rate of $\dot{P} = -0.029 \pm 0.008$ s yr^{-1}. However, S. Hoyer et al. (2016) ruled out the orbital decay of WASP-43b, reporting a period change rate of $\dot{P} = -0.02 \pm 6.6$ ms yr^{-1}, which is three orders of magnitude smaller than the value previously reported by I.-G. Jiang et al. (2016). K. B. Stevenson et al. (2017) also found no evidence for tidal decay. K. C. Patra et al. (2020) found a positive orbital change rate of $\dot{P} = (1.9 \pm 0.6) \times 10^{-10}$.

After the launch of the Transiting Exoplanet Survey Satellite (TESS), I. Wong et al. (2020) updated the transit ephemerides, providing an orbital period change of $\dot{P} < 5.6$ ms yr^{-1}. Recently, F. Davoudi et al. (2021) found a decrease in the orbital period of WASP-43b with a rate of -0.0035 ± 0.0007 s yr^{-1}. Moreover, Z. Garai et al. (2021a) conducted another study using TESS data combined with data from the Multicolor Simultaneous Camera for studying Atmospheres of

Transiting exoplanets 2 (MuSCAT2) and found the orbital period change rate of WASP-43b to be $\dot{P} = -0.6 \pm 1.2$ ms yr^{-1}, which is consistent with a constant-period value. Therefore, they confirmed that no orbital decay was detected in WASP-43b. Based on these developments, further investigation is needed to clarify TTVs of WASP-43 b, particularly regarding orbital decay.

Not only are the TTVs of WASP-43 b of interest, but extensive studies of its atmosphere have been conducted over the past decade. Focusing on WASP-43 b's emission spectra, the first eclipse data of WASP-43 b were obtained using the Spitzer Space Telescope's Infrared Array Camera (IRAC) at 3.6 and 4.5 μm (J. Blecic et al. 2014). The first complete orbital phase curve of WASP-43 b, obtained by Spitzer, was presented by K. B. Stevenson et al. (2017), revealing the presence of H_2O and CO+CO_2 and detecting variations in CH_4 emission spectra. More recently, F. Lesjak et al. (2023) presented the first high-resolution dayside spectra of WASP-43 b and detected the presence of CO and H_2O abundances. Following the launch of the James Webb Space Telescope (JWST), T. J. Bell et al. (2023) provided a full phase curve of WASP-43 b, observed using the Mid-Infrared Instrument (MIRI) in low resolution spectroscopy (LRS) mode on the JWST. The data were analyzed in T. J. Bell et al. (2024), showing a significant day −night temperature contrast in the spectrum and evidence of water absorption at all orbital phases.

For the transmission spectra of WASP-43 b, the first study of transmission spectra of WASP-43 b was conducted using the Wide Field Camera 3 (WFC3) on the Hubble Space Telescope (HST; L. Kreidberg et al. 2014), providing initial evidence for the presence of H_2O in its atmosphere. These HST transmission data were later reanalyzed by A. Tsiaras et al. (2018), who identified evidence of H_2O, with a log volume mixing ratio of -4.36 ± 2.10 and a cloud-top pressure of 2.90 ± 2.12. Moreover, I. C. Weaver et al. (2020) presented ground-based transmission spectrum data for WASP-43 b from the ACCESS Survey; however, no significant presence of Na, K, or Hα was detected. K. L. Chubb et al. (2020) also reanalyzed the same HST transmission dataset, reporting evidence of AlO in transmission with a high significance level ($>5\sigma$) compared to a flat model. D. Bartelt et al. (2025) observed four transits of WASP-43 b using the high-resolution Immersion GRating InfraRed Spectrometer (IGRINS) on the Gemini-S telescope, measuring a water abundance of $\log_{10}(H_2O) = -2.24^{+0.57}_{-0.48}$ without detecting any other carbon-bearing species.

In this work, we present a decade of ground-based multiband photometric follow-up observations comprising 35 transits of WASP-43 b from the SPEARNET telescope network, a ground-based transmission spectroscopy survey (J. J. C. Hayes et al. 2024). This extensive dataset enables robust constraints on the transit ephemeris and orbital decay. The details of these observations, combined with HST, TESS, JWST, and other published data, are provided in Section 2. Aligning with the objectives of SPEARNET, we perform a homogeneous analysis of all light curves using the `TransitFit` package to ensure parameter reliability and avoid inconsistencies arising from heterogeneous literature values, as detailed in Section 3. In Section 4, the derived midtransit times are used to constrain a new linear ephemeris and investigate orbital decay and TTV signals. Additionally, the transit depths from the multiband observations are analyzed to constrain the atmospheric composition of WASP-43 b in Section 5. Finally, the discussion and conclusion are presented in Section 6.

2. Observational Data

In this work, we combined photometric light-curve data spanning optical to mid-infrared wavelengths, including our observational data, published ground-based data, and data from HST, TESS, and JWST. The details are provided in the following sections.

2.1. SPEARNET Observations and Data Reduction

Multiband photometric follow-up observations of WASP-43 b were conducted between 2017 March and 2022 February using the SPEARNET telescope network (J. J. C. Hayes et al. 2024). In total, transit photometry was obtained for 35 transits, comprising 28 full and 7 partial transits. The observation log and details of the SPEARNET facilities are provided in Table 1. Details of the specific telescopes used in this work are provided below:

1. *2.4 m Thai National Telescope (2.4 m TNT)* is located at the Thai National Observatory (TNO) in Thailand; we obtained multiband photometric data for five full transits and one partial transit of WASP-43 b using the 2.4 m TNT between 2018 and 2021. The observations were performed with ULTRASPEC (V. S. Dhillon et al. 2014), a high-speed frame transfer EMCCD camera with 1024 × 1024 pixels and a field of view of 7.68 × 7.68 arcmin^2.
2. *0.5 m Thai Robotic Telescope at the Thai National Observatory (TRT-TNO), Thailand.* In 2017, we observed two full transits and one partial transit of WASP-43 b using the 0.5 m Schmidt–Cassegrain TRT-TNO. The observations were conducted with an Andor iKon-M 934 CCD camera (1024 × 1024 pixels), which features a field of view of approximately 23.4 × 23.4 arcmin^2.
3. *1 m Thai National Telescope (1 m TNT)* is located at TNO. The 1 m TNT is an upgraded version of the 0.5 m telescope at TNO. Starting in 2021, we observed six full transits of WASP-43 b using the 1 m Schmidt–Cassegrain telescope. The observations were conducted with an Andor iKon-M 934 CCD camera (1024 × 1024 pixels), which provides a field of view of approximately 23.4 × 23.4 arcmin^2.
4. *0.7 m Thai Robotic Telescope at the Gao Mei Gu Observatory (TRT-GAO), China.* Two full transit light curves of WASP-43 b were obtained by the TRT-GAO between 2017 and 2019. The observations were conducted using an Andor iKon-L 936 CCD camera equipped with a 2048 × 2048 pixel sensor. The camera provides a field of view of 20.9 × 20.9 arcmin^2.
5. *0.7 m Thai Robotic Telescope at the Spring Brook Observatory (TRT-SBO), Australia.* WASP-43 b was observed by TRT-SBO between 2019 and 2021. During this period, six full transits and two partial transits were recorded. The TRT-SBO is equipped with a 4096 × 4096 pixel ProLine PL16803 Monochrome CCD camera, providing a field of view of 28 × 28 arcmin^2.
6. *0.7 m Thai Robotic Telescope at the Sierra Remote Observatories (TRT-SRO), USA.* One full transit light curve of WASP-43 b was obtained by TRT-SRO in 2022. The observation was conducted using an Andor iKon-M 934 CCD camera with a 1024 × 1024 pixel sensor, providing a field of view of 20.9 × 20.9 arcmin^2.

Table 1
Observation Log of WASP-43 b Transits Observed with the SPEARNET Telescopes

Observation Date	Epoch[a]	Telescope	Filter	Exposure Time (s)	Number of Images	Total Duration of Observation (hr)	PNR (%)[b]	Transit Coverage
2017 Mar 04	484	0.7 m ROP-NM	*R*	20	128	2.40	0.25	Full
	484	0.7 m ROP-NM	*V*	35	131	2.45	0.37	Full
2017 Mar 13	495	0.7 m ROP-NM	*R*	60	111	2.59	0.34	Full
	495	0.7 m TRT-GAO	*R*	20	102	0.70	0.25	Full
	495	0.5 m TRT-TNT	*I*	20	220	1.72	0.49	Egress only
2017 Mar 21	505	0.7 m ROP-NM	*R*	20	270	2.21	0.18	Full
	505	0.5 m TRT-TNT	*I*	20	258	1.76	0.41	Full
2017 Mar 30	516	0.5 m TRT-TNT	*I*	20	461	2.89	0.35	Full
2018 Jan 29	891	2.4 m TNT	g'	12.83	864	3.08	0.14	Full
2018 Feb 02	896	2.4 m TNT	r'	3.56	535	1.60	0.17	Ingress only
2018 Feb 07	902	0.7 m ROP-NM	*V*	70	17	1.99	0.25	Egress only
	902	0.7 m ROP-NM	*R*	70	17	1.35	0.28	Egress only
	902	0.7 m ROP-NM	*I*	70	23	1.86	0.32	Egress only
2018 Feb 16	913	0.7 m ROP-CC	*R*	30	217	2.13	0.39	Full
2018 Mar 01	926	2.4 m TNT	i'	2.16	3289	2.81	0.17	Full
2018 Mar 23	956	2.4 m TNT	z'	12.78	850	3.12	0.15	Full
2019 Jan 21	1330	2.4 m TNT	r'	3.51	2482	2.43	0.09	Full
2019 Feb 09	1353	0.7 m TRT-SBO	*I*	60	232	5.46	0.32	Full
2019 Feb 13	1358	0.7 m TRT-SBO	*I*	60	78	1.73	0.31	Full
2019 Feb 22	1369	0.7 m ROP-CC	*V*	30	315	3.74	0.37	Full
2019 Mar 07	1385	0.7 m TRT-SBO	*I*	60	73	3.62	0.22	Full
2019 Apr 11	1428	0.7 m TRT-GAO	*R*	60	170	3.97	0.22	Full
2019 Apr 16	1434	0.7 m TRT-SBO	*I*	60	183	3.77	0.30	Full
2020 Dec 11	2178	0.7 m TRT-SBO	*R*	40	126	1.93	0.25	Full
2021 Jan 18	2225	1 m TNT	*R*	3	707	2.06	0.15	Full
2021 Jan 19	2226	0.7 m TRT-SBO	*R*	40	125	1.99	0.21	Ingress only
2021 Jan 23	2231	1 m TNT	*R*	3	857	2.67	0.12	Full
2021 Feb 09	2252	1 m TNT	*R*	3	1031	3.12	0.14	Full
2021 Feb 10	2253	0.7 m TRT-SBO	*R*	31	73	3.11	0.21	Full
2021 Feb 15	2259	0.7 m TRT-SBO	*R*	31	26	1.56	0.12	Ingress only
2021 Mar 17	2296	1 m TNT	*R*	3	652	1.83	0.12	Full
	2296	2.4 m TNT	r'	2.19	2774	1.70	0.20	Full
2021 Dec 07	2622	1 m TNT	*V*	5	1201	3.60	0.14	Full
2021 Dec 20	2638	1 m TNT	*V*	5	943	3.00	0.15	Full
2022 Feb 09	2700	0.7 m TRT-SRO	*R*	30	208	2.53	0.37	Full

Note.
[a] Epoch = 0 is the transit on 2016 February 4.
[b] PNR is the photometric noise rate (B. J. Fulton et al. 2011).

7. *0.7 m Regional Observatory for the Public Nakhon Ratchasima (ROP-NM), Thailand.* During 2017–2018, the 0.7 m ROP-NM obtained four full and three partial transit light curves of WASP-43 b. The observations were conducted using a 4096 × 4096 pixel ProLine PL16803 Monochrome CCD camera, with a field of view of approximately 28 × 28 arcmin^2.
8. *0.7 m Regional Observatory for the Public Chachoengsao (ROP-CC), Thailand.* Two full transit light curves were obtained by the 0.7 m ROP-CC from 2018 to 2019. The observations were conducted using the ProLine PL16803 Monochrome CCD camera (4096 × 4096 pixels), providing a field of view of approximately 28 × 28 arcmin^2.

The SPEARNET multiband photometric observations were calibrated using standard tasks from `IRAF`[15] (D. Tody 1986, 1993). Astrometric calibrations were performed using `Astrometry.net` (D. Lang et al. 2010). Aperture photometry was carried out on all images using `SExtractor` (E. Bertin & S. Arnouts 1996). Reference stars were chosen from nearby stars within 3 mag of WASP-43 that exhibited no variations in brightness. Outlier points in the light curves were removed using a 5σ clipping algorithm. To generate the light curves, the flux of WASP-43 was divided by the sum of the flux from the selected reference stars. The time stamps were converted to Barycentric Julian Date in Barycentric Dynamical Time (BJD_{TDB}) using `barycorrpy` (S. Kanodia & J. Wright 2018). The normalized light curves are available in a machine-readable format in Table 3.

2.2. Existing Ground-based Data

Since its discovery in 2011, WASP-43 b has been observed by a number of ground-based telescopes. In addition to the light curves from our observations, we utilized 109 ground-based transit light curves from eight previous studies. The published light curves, along with details of their instruments and filters, are listed in Table 2.

[15] IRAF is distributed by the National Optical Astronomy Observatories, which are operated by the Association of Universities for Research in Astronomy, Inc., under a cooperative agreement with the National Science Foundation (`http://iraf.noao.edu/`).

Table 2
WASP-43 b's Transit Light Curves Taken from Available Published Data for the Analyses

Sources	Telescope	Filter	Number of Light Curves	Epoch Span[a]
M. Gillon et al. (2012)	TRAPPIST	$I + z'$	19	(−2086, −2318)
	Euler	Gunn-r'	3	
G. Maciejewski et al. (2013)	2.2 m Calar Alto	R	1	−1789
	0.6 m Toruǹ	Clear	1	−1297
G. Chen et al. (2014)	MPG/ESO 2.2 m telescope	g'	1	−1830
		r'	1	
		i'	1	
		z'	1	
		J	1	
		H	1	
		K	1	
F. Murgas et al. (2014)	10.4 m GTC/OSIRIS	0.52–1.04 μm	34	−1379
D. Ricci et al. (2015)	1.5 m San Pedro Màrtir telescopes	i'	2	(−779,−887)
	0.84 m San Pedro Màrtir telescopes	V	2	
		R	2	
		I	2	
I.-G. Jiang et al. (2016)	P60 Palomar Observatory	R	7	(−469,−854)
H. Parviainen et al. (2019)	MuSCAT2	g'	3	(867,970)
		r'	3	
		i'	2	
		z'	3	
Z. Garai et al. (2021a)	MuSCAT2	g'	4	(916,1307)
		r'	5	
		i'	5	
		z'	4	
	TESS Sector 09	TESS	26	(1379, 1407)
	TESS Sector 35	TESS	24	(2253, 2282)
	TESS Sector 62	TESS	28	(3155, 3184)
	TESS Sector 89	TESS	33	(4051, 4083)
	HST/WFC3	G141 (1.1–1.7 μm.)	150	(−993, −1011)
	JWST/MIRI	P750L (5–12 μm.)	11	3063

Note.
[a] Epoch = 0 is the transit on 2016 February 4.

2.3. HST/WFC3 G141 Grism Data

WASP-43 b was observed by HST/WFC3 as part of Proposal ID 13467 (P.I. Jacob Bean; L. Kreidberg et al. 2014). During the observation period from 2013 November 4 to 19, six transits were observed using the G141 grism, covering the wavelength range from 1.1 to 1.7 μm. In this work, the HST/WFC3 raw spectra of WASP-43 b were downloaded from the Exo.MAST[16] database. The data reduction was performed using the `Iraclis` package, a Python tool for the WFC3 spectroscopic reduction pipeline (A. Tsiaras et al. 2016a, 2016b). The G141 grism spectra were binned into 25 wavelength bins, resulting in a total of 150 light curves obtained from HST/WFC3. Data from the first orbit of each visit and the first exposure of each orbit were discarded owing to the presence of a stronger wavelength-dependent ramp during these epochs (A. Tsiaras et al. 2016a).

2.4. TESS Data

TESS observed WASP-43 b in four time intervals, yielding a total of 26 transit light curves from Sector 09 (2019 February 28–March 26), 24 light curves from Sector 35 (2021 February 9–March 7), 28 light curves from Sector 62 (2023 February 12–March 9), and 33 light curves from Sector 89 (2025 February 12–March 10). These light curves were downloaded from the Mikulski Archive for Space Telescopes (MAST).[17] We used the Pre-Search Data Conditioning (PDC) light curves, which are

[16] Downloaded from Exo.MAST: https://exo.mast.stsci.edu/.

[17] Downloaded from the Mikulski Archive for Space Telescopes: https://archive.stsci.edu/.

the calibrated data provided by the Science Processing Operation Center (SPOC) pipeline (J. M. Jenkins et al. 2016).

2.5. JWST Data

A full orbit of WASP-43 b was observed by JWST on 2022 December 1 as part of the Transiting Exoplanet Community Early Release Science Program (JWST-ERS-1366), led by PI Taylor J. Bell (T. J. Bell et al. 2023, 2024). The observation utilized the JWST MIRI in LRS slitless mode with the P750L filter, covering a wavelength range from 5 to 12 μm. We used the 11 available JWST light curves reduced by `Eureka!v1` (T. Bell et al. 2022) from T. J. Bell et al. (2024).

3. TransitFit Light-curve Modeling

To determine the planetary parameters of WASP-43 b, we used `TransitFit`, a Python package designed for fitting multifilter and multiepoch exoplanet transit observations simultaneously (J. J. C. Hayes et al. 2024). The package employs the transit model from `batman` (L. Kreidberg 2015) and utilizes dynamic nested sampling routines from `dynesty` (J. S. Speagle 2020) to derive the parameters.

As mentioned in Section 2, we utilized a large number of light curves from both ground-based and space-based observations. To mitigate issues related to computer memory, we divided the light-curve data into four distinct groups: ground-based, HST, TESS, and JWST datasets. The light curves from each group were simultaneously fitted and detrended using `TransitFit`.

For the light-curve detrending, each transit light curve was individually detrended using different detrending functions. We applied second-order polynomial detrending functions for the ground-based, TESS, and JWST datasets. The normalized light curves from our SPEARNET ground-based observations are shown in Table 3. For the HST/WFC3 G141 data, we used a custom detrending function implemented in `TransitFit`. This detrending function was based on the method described by L. Kreidberg et al. (2018), specifically designed for the WFC3 data,

$$F_{\rm sys} = (S + v_1 t_{\rm visit} + v_2 t_{\rm visit}^2)(1 - e^{-{\rm at}_{\rm orb} - b}), \quad (1)$$

where $F_{\rm sys}$ is the signal from the systematics, where $S = 1$ and $S = s$ for forward and reverse scans, respectively. The parameters s, v_1, v_2, a, and b are detrending coefficients, with s, a, and b accounting for the ramp-up systematic across all the light curves, while v_1 and v_2 are the second-order polynomial detrending functions used to model the visit-long trends. The time elapsed since the first exposure in the visit is represented as $t_{\rm visit}$, and the time elapsed since the first exposure in the orbit is presented as $t_{\rm orb}$. The astrophysical signal ($F_{\rm sig}$) can be obtained by dividing the observed flux ($F_{\rm obs}$) by the systematic signal ($F_{\rm sys}$).

To perform the `TransitFit` fitting, we used a stellar effective temperature for the host star of WASP-43 b of $T = 4166 \pm 100$ K, calculated using the Python Stellar Spectral Energy Distribution package.[18] This tool set is designed to allow the user to create, modify, and fit the spectral energy distributions of stars based on publicly available data (I. McDonald et al. 2009, 2012, 2017). The host metallicity, $Z_* = -0.05 \pm 0.17$, from A. S. Bonomo et al. (2017) and surface gravity, $\log(g_*) = 4.6 \pm 0.1$, from the Gaia EDR3 catalog[19] were used. To find the best fit for all light curves from the four different datasets, we assumed that the orbit of WASP-43 b is circular. The priors for each parameter —orbital period (P in days), midtransit for each epoch (T_m in BJD), orbital inclination (i in deg), semimajor axis (a in units of stellar radius, R_*), and the planet's radius (R_p in units of stellar radius, R_*)—for each filter are given in Table 4.

Since WASP-43 b was observed over several years, its orbital period might not be constant. Therefore, we first determined the best value for the orbital period P. The prior for the orbital period, with a Gaussian distribution of $0.813474 \pm 1 \times 10^{-6}$ days, was used to calculate the best orbital period for each dataset. The parameters for inclination i and semimajor axis a were allowed to vary. The best-fit values for the inclination, semimajor axis, and orbital period, obtained from the analysis of each dataset, are given in Table 5. From the analysis, the best-fit values from each dataset are combined

Table 3
The Detrended Transit Light Curves of WASP-43 b, Observed by the Telescopes within the SPEARNET Network

Epoch	BJD	Normalized Flux	Normalized Flux Error
484	2457817.13376	1.001	0.007
	2457817.13442	0.996	0.007
	2457817.13508	1.002	0.006
	…	…	…
495	2457826.08193	0.988	0.005
	2457826.08220	0.999	0.005
	2457826.08248	0.994	0.005
	…	…	…
505	2457834.22363	1.000	0.003
	2457834.22440	0.993	0.002
	2457834.22466	0.998	0.002
	…	…	…
…	…	…	…

(This table is available in its entirety in machine-readable form in the online article.)

Table 4
The Priors Used to Model the Planetary Parameters of WASP-43 b for the Analysis of All Ground-based, TESS, JWST, and HST/WFC3 Light Curves with `TransitFit`

Parameter	Priors	Prior Distribution
P (days)	$0.813474 \pm 1 \times 10^{-6}$	Gaussian
t_0 (BJD)	2457423.45 ± 0.002	Gaussian
i (deg)	(80, 84)	Uniform
a/R_*	(4,6)	Uniform
R_p/R_*	(0.14, 0.17)	Uniform
e	0	Fixed
T_* (K)	4166 ± 100	Fixed
Z_*	-0.05 ± 0.17	Fixed
$\log(g_*)$	4.6 ± 0.1	Fixed

Note. The priors of P, i, and a/R_* are set to the values in C. Hellier et al. (2011), and t_0 is set to the value in E. S. Ivshina & J. N. Winn (2022).

[18] Python Stellar Spectral Energy Distribution package on https://explore-platform.eu/.

[19] Gaia archive: `https://archives.esac.esa.int/gaia`.

Table 5
The Best-fit Values of the Planetary Parameters of WASP-43 b for All Four Datasets Modeled with `TransitFit`

References	P (days)	i (deg)	a/R_*
C. Hellier et al. (2011)	$0.813475 \pm 1 \times 10^{-6}$	$82.6^{+1.3}_{-0.9}$	4.97 ± 0.14
A. S. Bonomo et al. (2017)	$0.81347437 \pm 1.3 \times 10^{-7}$	82.33 ± 0.20	...
A. Kokori et al. (2023)	$0.813474056 \pm 2.1 \times 10^{-8}$	82.11 ± 0.10	4.867 ± 0.023
This Study			
Ground-based	$0.81347420 \pm 1 \times 10^{-8}$	81.89 ± 0.02	4.799 ± 0.005
HST	$0.81347442 \pm 7 \times 10^{-8}$	82.35 ± 0.02	4.896 ± 0.005
TESS	$0.81347406 \pm 1 \times 10^{-8}$	82.03 ± 0.06	4.83 ± 0.02
JWST	$0.8134739 \pm 1 \times 10^{-7}$	82.04 ± 0.02	4.839 ± 0.004
Weighted mean values	$0.813474131 \pm 7 \times 10^{-9}$	82.12 ± 0.01	4.845 ± 0.003

using the weighted mean. The weighted mean parameters of WASP-43 b indicate an inclination of $82.^{\circ}12 \pm 0.^{\circ}01$ and a semimajor axis of $4.845R_* \pm 0.003R_*$. A comparison shows that the results of our study are compatible with previous measurements within 1σ.

The investigation of TTVs was conducted using the `allow_TTV` function in `TransitFit`. In this step, the weighted mean values of the orbital period, inclination, and semimajor axis, determined in the first step, were fixed to account for TTVs and the midtransit time (T_m) for each epoch. The planet's radius (R_p) and limb-darkening coefficients (LDCs) were allowed to vary. For the analysis of the LDCs for each filter, the fitting was performed using the `custom` LDC fitting mode in `TransitFit`. The prior LDC values for each filter were obtained from the Exoplanet Characterization Toolkit (ExoCTK; M. Bourque et al. 2021).[20] However, for the HST light-curve fitting, the LDCs were fixed owing to the gap between the orbital ingress and egress parts of the light curve. The limb-darkening parameters calculated using `TransitFit` show the same trend as those obtained from `ExoCTK`, with a difference of less than 0.2 for the first-order LDC (u_0).

The light curves were phase-folded with their best-fit models, and the residuals are shown in Figures 1, 2, C1, C2, and C3. The individual light-curve fittings for 23 TRT light curves, HST observations from 2013 November 04–19, and TESS observations in Sectors 35, 62, and 89 are presented in Appendix C. The midtransit times are provided in Table B1 and discussed in Section 4. The LDCs were fitted as free parameters using the quadratic limb-darkening model. The values of the LDCs for 58 different filters, derived from `TransitFit`, are listed in Table A1.

4. Timing Analysis

4.1. Ephemeris Refinement

To search for timing variations in WASP-43 b, the midtransit times of 188 epochs obtained from `TransitFit`, listed in Table B1, were analyzed. First, a new linear ephemeris was derived by fitting the midtransit times with a constant-period model as follows:

$$t_{0,c} = t_{0,l} + P_l \times E, \quad (2)$$

where $t_{0,l}$ and P_l are the reference time and the orbital period of the linear ephemeris model, respectively, E is the epoch number, and $E = 0$ represents the transit on 2016 February 4. Parameter $t_{0,c}$ is the calculated midtransit time at a given epoch E.

The fitting was conducted using `emcee` (D. Foreman-Mackey et al. 2013), which employs a Markov Chain Monte Carlo (MCMC) algorithm with 50 chains and 10^5 MCMC steps to determine the optimal parameters for the model. A summary of the priors used and the best-fit model parameters is presented in Table 6. The new defined linear ephemeris is as follows:

$$t_{0,c} = 2457423.44976^{+0.00003}_{-0.00003} + 0.81347406^{+1\times10^{-8}}_{-1\times10^{-8}}E. \quad (3)$$

The reduced chi-square for the linear model is $\chi^2_{\rm red} = 18.8$ with 186 degrees of freedom. The Bayesian information criterion (BIC) is calculated as $\mathrm{BIC} = \chi^2 + k \ln n = 3511$, where k represents the number of free parameters and n is the number of data points. The corner plot of the MCMC posterior distribution is shown in Figure D1. Using this new linear ephemeris, we constructed the $O - C$ diagram of WASP-43 b (Figure 3), which displays the timing residuals ($O - C$) between the observed timing data and the linear Equation (3).

4.2. Orbital Decay Investigation

WASP-43 b remains a good candidate for observing orbital decay, due to its ultrashort orbital period, although Z. Garai et al. (2021a) have highlighted the orbital decay of WASP-43 b with unresolved conclusions. The orbital decay of WASP-43 b was investigated in this work. The timing data for a total of 188 epochs were also fitted with the orbital decay model using the following equation:

$$t_{0,c} = t_{0,d} + E \times P_d + \frac{1}{2}\frac{dP_d}{dE}E^2, \quad (4)$$

where $t_{0,d}$ is a reference time of the orbital decay model. P_d is planetary orbital period of the orbital decay model, and dP_d/dE is the change in the orbital period per orbit.

The fitting for the orbital decay model was performed using the MCMC routine. The priors used and the best-fitting model are provided in Table 6, with the posterior distribution of the MCMC shown in Figure D1. From the best-fit parameters, the timing residuals as a function of epoch E for the orbital decay model, obtained by subtracting the best-fitting constant-period model, are shown in Figure 3. We obtained the change in the orbital period, $dP_d/dE = -3^{+1}_{-1} \times 10^{-11}$ days/orbit, with the reduced chi-square of the model $\chi^2_{\rm red} = 18.3$ (185 degrees of freedom) and $\mathrm{BIC} = 3408$.

[20] ExoCTK limb-darkening calculator: https://exoctk.stsci.edu/limb_darkening.

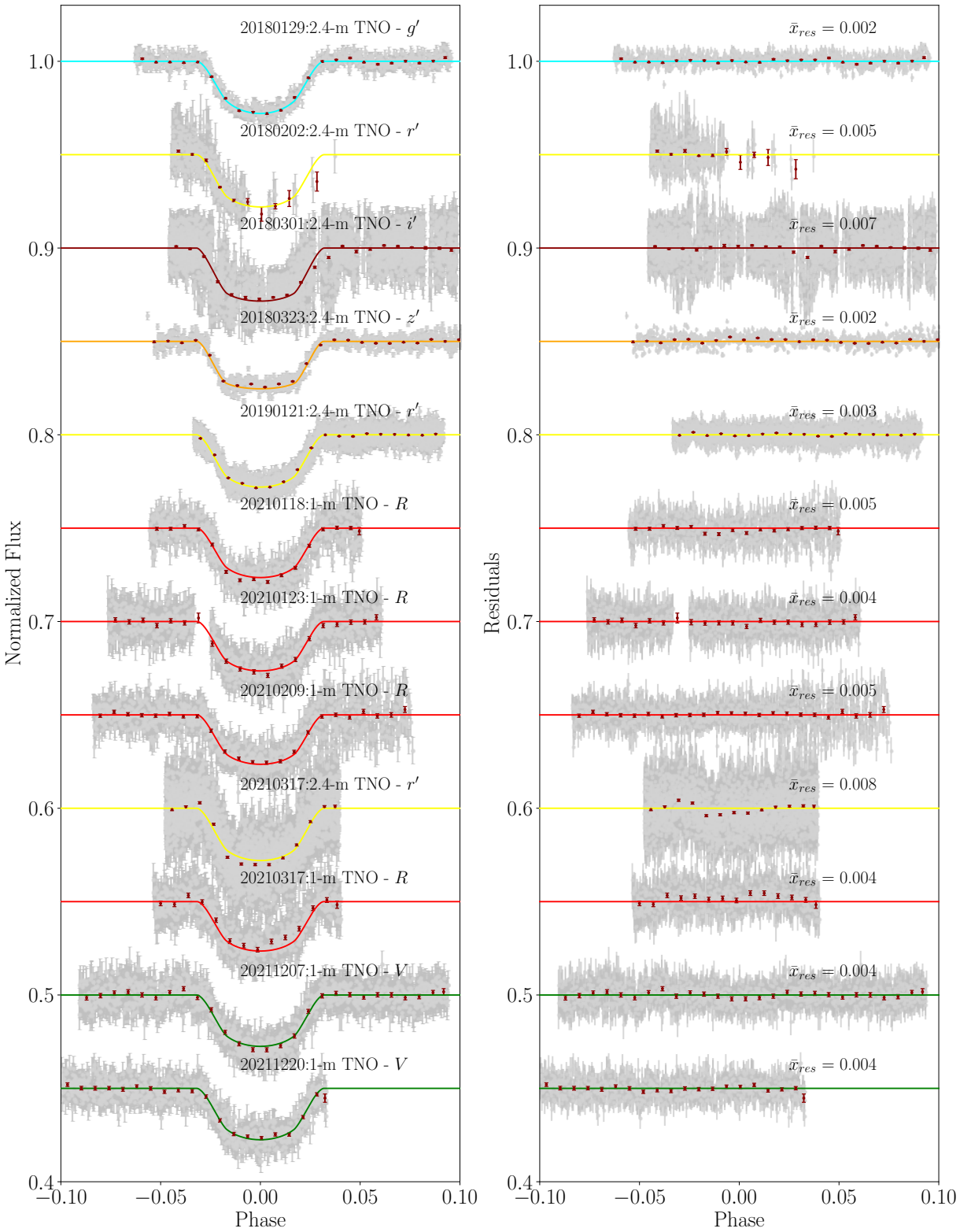

Figure 1. Left panels: the normalized, phase-folded transit light curves of WASP-43 b from the 2.4 m and 1 m TNT observations in the SPEARNET telescope network, shown as gray circles. The best-fitting model from `TransitFit` is displayed as a solid line. Right panels: residuals of the light curves after model subtraction. Both the light curves and residuals are vertically offset for clarity. The corresponding residuals and the mean residual values ($\bar{x}_{\rm res}$) with clear offsets are displayed in the right panel.

Since the values of $\chi^2_{\rm red}$ and BIC from both the constant-period model and the orbital decay model in our analysis do not show a significant difference, there is no strong evidence for the detection of orbital decay in WASP-43 b.

4.3. Searching for the Periodicity in Timing Data

In order to investigate the periodicity of the timing residual ($O - C$) data for WASP-43 b, shown in Table 6, we used the Generalized Lomb–Scargle (GLS) periodogram (M. Zechmeister

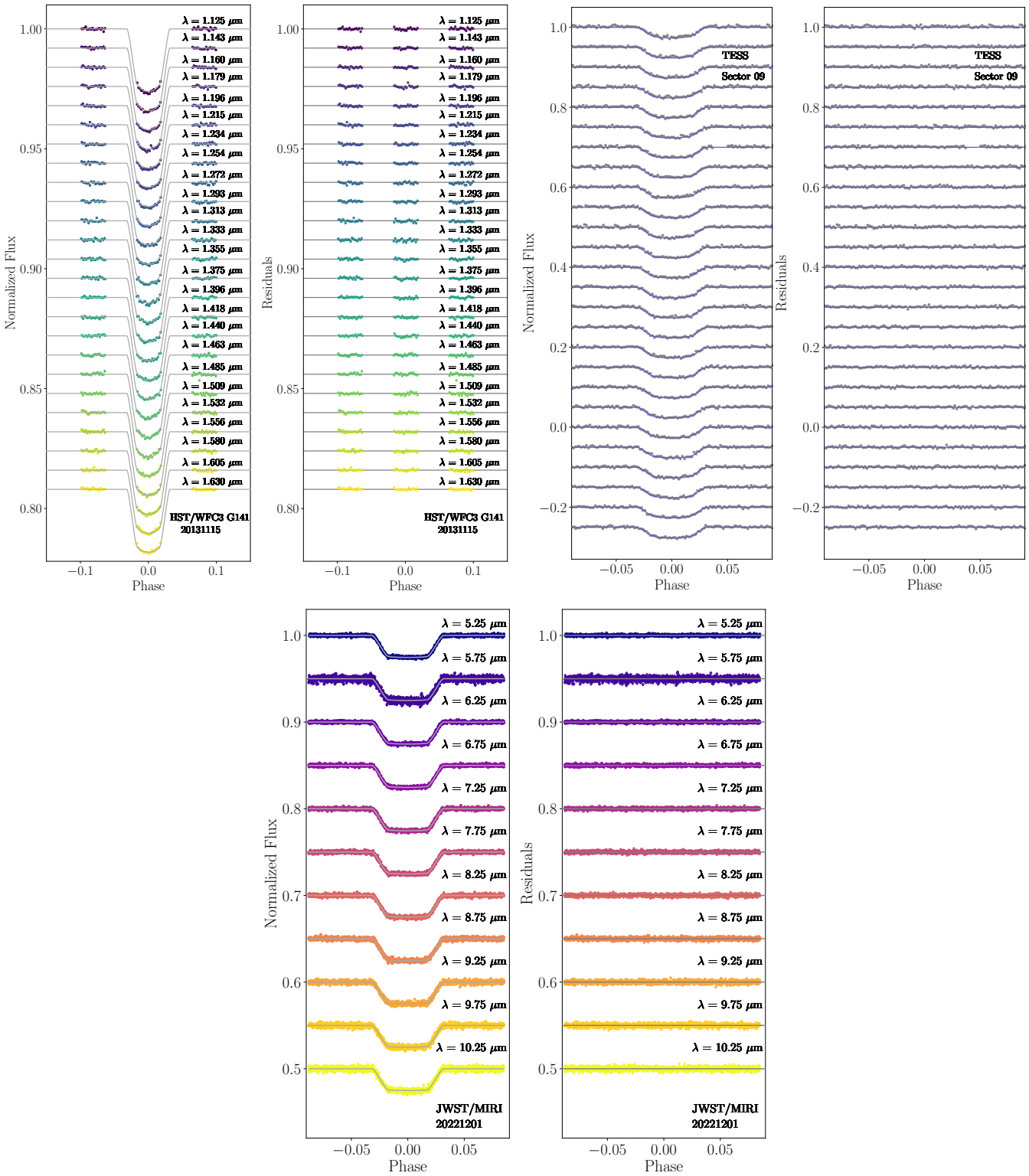

Figure 2. The normalized, phase-folded transit light curves of WASP-43 b are shown for HST/WFC3 G141 observations on 2013 November 15 (top left), TESS observations within Sector 9 (top right), and JWST/MIRI (bottom). The observational data are presented as circles, and the best-fitting model from `TransitFit` is shown as solid lines. Both the light curves and the corresponding residuals (right panels) are vertically offset for clarity.

& M. Kürster 2009) in the `PyAstronomy`[21] routines (S. Czesla et al. 2019). The GLS analysis was performed on all 188 timing residual ($O - C$) data points. The periodogram showed the highest power peak of 0.25 at a frequency of 0.01657 ± 0.00001 cycles day^{-1}, which corresponds to a false-alarm probability (FAP) of 9×10^{-7}% (Figure 4). Given the high obtained FAP values, no significant TTV signals were detected in our analysis.

The TESS transits in Sectors 09 and 35 were investigated for a downward trend in the orbital period by F. Davoudi et al. (2021).

[21] PyAstronomy: https://github.com/sczesla/PyAstronomy.

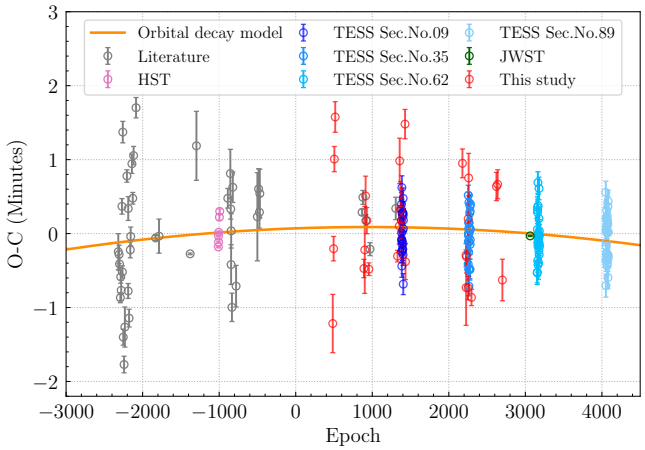

Figure 3. The $O - C$ diagram and best-fitting timing models for WASP-43 b, including data from the literature (gray circles), HST (pink circles), TESS (blue circles), JWST (green circles), and this study (red circles), are shown. The orange line represents the timing residuals of the orbital decay model.

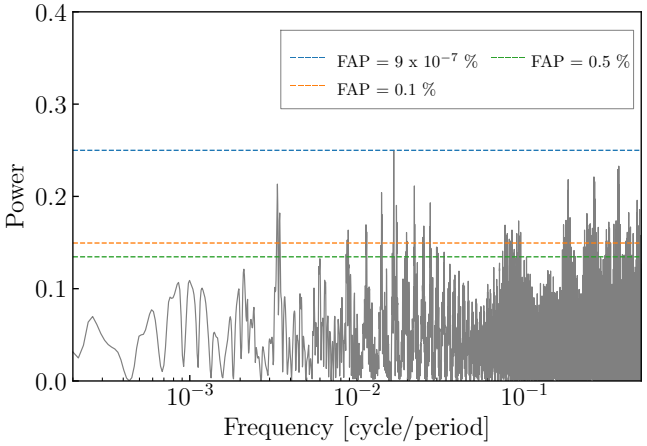

Figure 4. The GLS periodograms were calculated for the timing residuals of a total of 188 epochs. The dashed line indicates the FAP levels. The highest power peak was found at a frequency of 0.01657 ± 0.00001 cycles day^{-1}, with an FAP of 9 × 10^{-7}%.

Table 6
The Priors Used, the Uniform Distribution, and the Best-fitting Parameters from the MCMC for Both the Constant-period and Orbital Decay Models

Parameter	Uniform Distribution Priors	Best-fit Values
	Constant-period Model	
$P_{\mathrm{orb},l}$ (days)	(0.81347,0.81348)	$0.81347406^{+1\times10^{-8}}_{-1\times10^{-8}}$
$t_{0,l}$ ($\mathrm{BJD_{TDB}}$)	(2457423.445, 2457423.453)	$2457423.44976^{+0.00003}_{-0.00003}$
χ^2_{red}	18.8	
BIC	3511	
	Orbital Decay Model	
$P_{\mathrm{orb},d}$ (days)	(0.81347, 0.81348)	$0.81347409^{+2\times10^{-8}}_{-2\times10^{-8}}$
$t_{0,d}$ ($\mathrm{BJD_{TDB}}$)	(2457423.445, 2457423.453)	$2457423.44981^{+0.00004}_{-0.00004}$
dP / dE (days/ orbit)	(-0.2, 0.2)	$-3^{+1}_{-1} \times 10^{-11}$
χ^2_{red}	18.3	
BIC	3408	

They found a decrease in the orbital period of $(-1.15 \pm 0.76) \times 10^{-7}$ in the slope line between a 2 yr interval of TESS observations, suggesting that the target is more interesting for follow-up observations. Motivated by this, we performed a timing variation analysis for these TESS timing residual ($O - C$) data, including the latest TESS data from Sectors 62 and 89. The $O - C$ data derived for TESS data are shown in Figure 5. Similar to the total of 188 $O - C$ data points, the $O - C$ of the TESS data was searched for timing variability over a 5 yr interval. Using GLS, the periodogram shows the highest power peak of 0.142 at a frequency of 0.33017 ± 0.00005 cycles period^{-1} (epoch) with an FAP of 29.7% (Figure 6).

4.4. Upper Mass Limit for an Additional Planet

Since no TTV signal was detected from the timing data, the 188 midtransit times from `TransitFit` were used to simulate the upper mass limit of a potential nearby planetary companion. To estimate the upper mass limit of the second planet, we adapted the method described by S. Awiphan et al. (2016) and N. A-thano et al. (2022). The orbit of the second planet is assumed to be circular and coplanar with the orbit of WASP-43 b. We calculated the unstable regions from the mutual Hill sphere between WASP-43 b and the perturbing planet, as described by D. C. Fabrycky et al. (2012):

$$r_{\mathrm{H}} = \frac{a_{\mathrm{in}} + a_{\mathrm{out}}}{2}\left(\frac{M_{\mathrm{in}} + M_{\mathrm{out}}}{3M_{\star}}\right)^{1/3}, \quad (5)$$

where a_{in} and a_{out} are the semimajor axis of the inner and outer planets (perturber planet), respectively. The boundary of stable orbit is when the separation of the planets' semimajor axes ($a_{\mathrm{out}} - a_{\mathrm{in}}$) is larger than $2\sqrt{3}$ of the mutual Hill sphere.

The TTV signal was computed using the `TTVFaster` package,[22] developed by K. M. Deck & E. Agol (2016), a tool for dynamical analysis. To obtain the accurate value of the TTV signal from `TTVFaster`, we employed the dynamic nested sampling algorithm from `dynesty` (J. S. Speagle 2020), using 200 live points and stopping when $\Delta \log Z = 0.5$. The period ratio between the second planet and WASP-43 b was varied from 0.3 to 4.50 with a step size of 0.01, while the mass range was set from 10^{-1} to 10^{3} $M_{\oplus}$ on a logarithmic scale. The initial phase of the second planet was allowed to vary between 0 and 2π. From the $O - C$ diagram in Figure 3, a signal amplitude of 15.40 s was found. We also calculated the upper mass limits corresponding to TTV amplitudes of 5, 15, and 25 s, as shown in Figure 7.

Then, we calculated the difference of the chi-square value ($\Delta\chi^2_{\mathrm{red}}$) by comparing the signal from the TTV model, representing the best fit for the two-planet model, χ^2_{red}, to the best-fit single-planet model or linear fitting model, with $\chi^2_{\mathrm{red},l}$ of 18.8. In Figure 7, the $\Delta\chi^2_{\mathrm{red}}$ is plotted as a function of the perturbing mass and period, showing that the lowest $\Delta\chi^2_{\mathrm{red}}$ values are close to the upper mass limit, corresponding to a TTV amplitude of 15 s. In the unstable orbit region with an orbital period ranging from 0.49 to 1.36 days, the presence of a second nearby planet is excluded. Based on the simulation, we can conclude that no planet with a mass heavier than 10^2 $M_{\oplus}$ exists with a period of less than 2 days.

[22] TTVFaster: https://github.com/ericagol/TTVFaster.

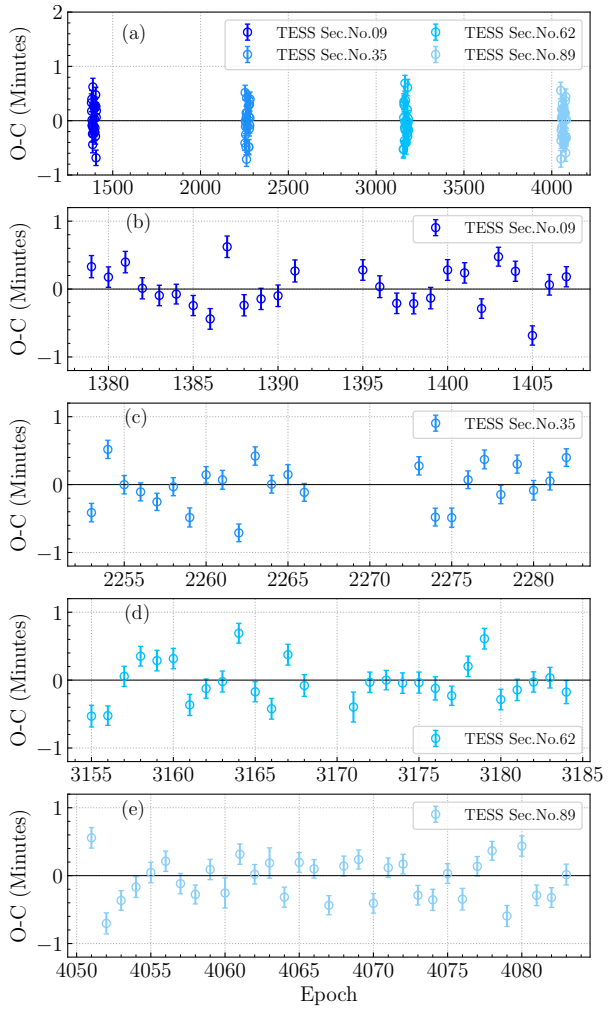

Figure 5. The $O - C$ diagram for the TESS datasets. (a) The $O - C$ data from observations in TESS three sectors over a 5 yr interval. (b–e) The $O - C$ data plotted by individual sectors for clearer visibility.

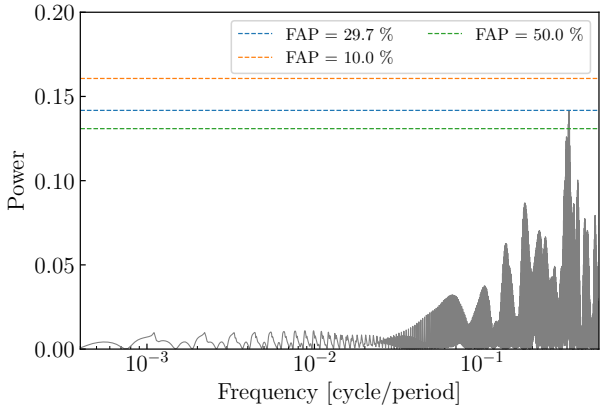

Figure 6. The GLS periodograms of the timing residuals for TESS data show that the highest power peak was found at a frequency of 0.33017 ± 0.00005 cycles day^{-1} with an FAP of 29.7%.

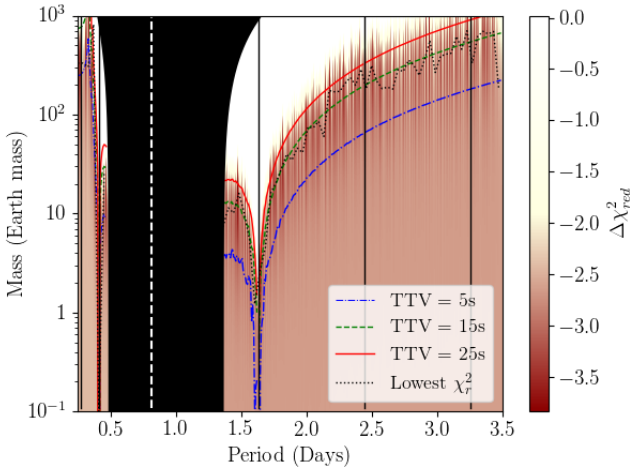

Figure 7. Upper mass limit of the perturbing planet in the WASP-43 system. The best $\Delta\chi^2_{\rm red}$ values, binned with a period ratio of 0.05, are shown as the black dotted line. The upper mass limits for TTV amplitudes of 5, 15, and 25 s are represented by the blue dashed–dotted, green dashed, and red solid lines, respectively. The white vertical line represents the orbital period of WASP-43 b. The black vertical lines, from left to right, indicate the orbital period resonances of 2:1, 1:2, 1:3, and 1:4. The contour illustrates the $\Delta\chi^2_{\rm red}$ values from comparing the best TTV model to the best linear model. The unstable orbit region is shown as the shaded black area.

5. WASP-43 b's Planetary Atmosphere

The transit depth data ranging from optical to mid-infrared wavelengths, derived from the light-curve fitting in Section 3, are used to reexamine the chemical compositions of WASP-43 b's atmosphere. In previous studies, the transmission spectrum of WASP-43 b obtained from HST/WFC3 G141 was utilized to determine the atmospheric composition, with the presence of H_2O detected by L. Kreidberg et al. (2018), A. Tsiaras et al. (2018), and I. C. Weaver et al. (2020). Furthermore, K. L. Chubb et al. (2020) analyzed the transmission spectrum provided by L. Kreidberg et al. (2018) and reported a highly significant detection of AlO, with a confidence level exceeding 5σ compared to a flat baseline model. Therefore, we first focus on the transit depth data from HST/WFC3 G141 to compare the results obtained from `TransitFit` with those from previous studies.

To retrieve the transmission spectrum of WASP-43 b, the open-source Bayesian atmospheric retrieval framework `TauREx3` (A. F. Al-Refaie et al. 2021),[23] was used with the nested sampling routines from `MultiNest` (F. Feroz et al. 2009) with 1000 live points to determine the atmospheric parameters. For the transmission spectrum modeling with the `TauREx3` package, the stellar parameters and planetary mass of the WASP-43 host star were taken from M. Esposito et al. (2017). The stellar spectrum for the host star, with a temperature of $T_* = 4166$ K, was simulated using a `PHOENIX` model (T. O. Husser et al. 2013). An isothermal temperature profile was assumed, using a plane-parallel atmosphere consisting of 100 layers. The cloud-top pressure was allowed to vary from 10^1 to 10^6 Pa on a logarithmic scale. A He/H_2 ratio of 0.17, consistent with the solar abundance, was used. The transmission spectra were generated at a resolution of 10,000 before being binned to match the instrumental resolution.

Following the initial study of the transmission spectrum of WASP-43 b by L. Kreidberg et al. (2018), we modeled the transmission spectrum by considering molecular opacities as described by L. Kreidberg et al. (2014). Specifically, H_2O (O. L. Polyansky et al. 2018), CH_4 (S. N. Yurchenko et al. 2024), CO (K. L. Chubb et al. 2021), CO_2 (S. N. Yurchenko et al. 2020), and AlO (A. T. Patrascu et al. 2014) were

[23] `TauREx3`: https://taurex3.readthedocs.io/en/latest/.

Table 7
Parameters and Their Priors Used in TauREx 3 Retrieval, Along with the Best-fit Retrieved Values with 1σ Uncertainties for Six Case Studies

Parameter	Priors	Scale	Retrieved Values					
			Case I	Case I.I	Case I.II	Case II	Case III	Case IV
T (K)	(200, 2000)	linear	900^{+500}_{-400}	500^{+200}_{-100}	1200^{+300}_{-300}	1200^{+200}_{-100}	400^{+100}_{-20}	400^{+20}_{-40}
H_2O	(-4.0, -1.0)	log	$-0.5^{+0.3}_{-2.3}$	-2^{+1}_{-2}	$-0.4^{+0.1}_{-0.2}$	$-0.5^{+0.1}_{-0.1}$	$-2.8^{+0.5}_{-1.2}$	$-2.1^{+0.3}_{-0.4}$
CH_4	(-9.0, -1.0)	log	-6^{+3}_{-3}	-5^{+2}_{-3}	-6^{+3}_{-3}	-6^{+3}_{-2}	-7^{+2}_{-2}	-8^{+2}_{-1}
CO	(-9.0, -1.0)	log	-6^{+3}_{-3}	-6^{+3}_{-3}	-6^{+3}_{-3}	-6^{+3}_{-3}	-7^{+2}_{-2}	-4^{+1}_{-3}
CO_2	(-9.0, -1.0)	log	-6^{+3}_{-3}	-6^{+3}_{-3}	-6^{+3}_{-3}	-6^{+3}_{-3}	-6^{+2}_{-3}	-6^{+2}_{-2}
TiO	(-9.0, -1.0)	log	-6^{+3}_{-3}	-6^{+2}_{-3}	-6^{+3}_{-3}	-6^{+2}_{-2}	$-9.5^{+0.7}_{-0.4}$	$-9.5^{+0.7}_{-0.4}$
VO	(-9.0, -1.0)	log	-8^{+2}_{-1}	-8^{+2}_{-1}	-8^{+2}_{-2}	-8^{+1}_{-1}	$-6.2^{+0.4}_{-1.1}$	$-6.1^{+0.4}_{-0.4}$
AlO	(-9.0, -1.0)	log	-6^{+2}_{-2}	-6^{+2}_{-2}	-7^{+2}_{-2}	-7^{+2}_{-2}	$-6.6^{+0.7}_{-0.8}$	-8^{+1}_{-1}
$\log(P_{\rm clouds})$ (Pa)	$(10^1, 10^6)$	log	4^{+1}_{-2}	4^{+1}_{-1}	3^{+2}_{-2}	$2.7^{+2.0}_{-0.8}$	$5.1^{+0.5}_{-0.6}$	-5^{+1}_{-1}
	$\chi^2_{\rm red}$		1.70	1.95	1.39	5.41	34.35	34.29

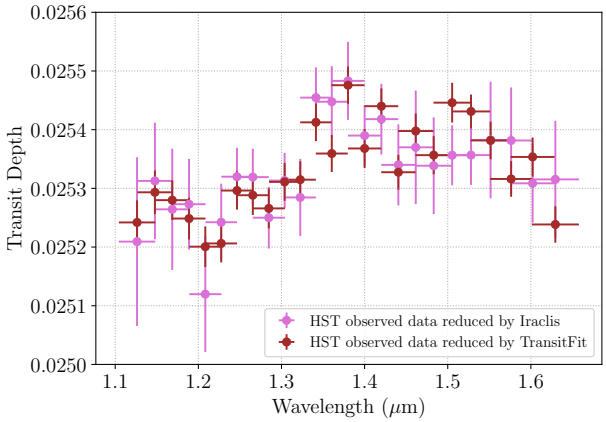

Figure 8. The HST transmission spectrum of WASP-43 b, reduced using Iraclis (pink) and TransitFit (dark red).

included. Additionally, we added potential metal oxides such as TiO (L. K. McKemmish et al. 2019) and VO (L. K. McKemmish et al. 2016) that have spectral features in the visible wave band in the model. The molecular line lists were obtained from the ExoMol (J. Tennyson et al. 2016), HITRAN (I. Gordon et al. 2016), and HITEMP (L. S. Rothman & I. E. Gordon 2014) databases. We also accounted for collision-induced absorption between H_2 molecules (M. Abel et al. 2011; L. N. Fletcher et al. 2018) and between H_2 and He (M. Abel et al. 2012). A list of priors for the parameters and chemical abundances used in the TauREx3 retrieval is provided in Table 7.

Previous studies have utilized TauREx3 to retrieve the atmospheric compositions of WASP-43 b using transmission spectra obtained via the Iraclis package (A. Tsiaras et al. 2016a), which uses PyLightcurve (D. Tody 2016) to fit the white light curve and correct systematics before fitting the spectral light curves. Adopting this framework, we analyzed the HST/WFC3 G141 data using the Iraclis package (Case I) and compared the results with transit depths derived using TransitFit (Case II). Furthermore, for the comprehensive atmospheric retrieval analysis, we combined these HST/WFC3 G141 datasets with transit depths in other wave bands derived from TransitFit, defining the combined Iraclis-based dataset as Case III and the combined TransitFit-based dataset as Case IV.

For the spectra obtained via the Iraclis package, we utilized the best-fit values of planetary parameters from Table 5. We analyzed both the Iraclis and TransitFit reductions to investigate the observed discrepancy in their transit depths, as shown in Figure 8. We determined that this difference arises primarily from the treatment of LDCs. Specifically, Iraclis utilizes LDCs from A. Claret (2000), whereas TransitFit employs LDCs derived from ExoCTK. Given that the choice of LDC models has a significant impact on the retrieved transit depths, we decided to include the analysis of both reductions to ensure a comprehensive comparison.

5.1. Case I: HST/WFC3 G141 Transmission Spectrum from Iraclis

For the fitting of the HST/WFC3 G141 transit light curves of WASP-43 b, we assumed a circular orbit. The orbital period (P), inclination (i), and semimajor axis (a) were taken from Table 5 and, along with the midtransit time ($t_0 = 2457423.44976$ $\rm BJD_{TDB}$), were fixed. The LDCs were modeled using the nonlinear four-coefficient law from A. Claret (2000). The host star parameters were defined consistently with the TransitFit light-curve analysis, adopting an effective temperature of $T = 4166 \pm 100$ K and metallicity $Z = -0.05 \pm 0.17$ from A. S. Bonomo et al. (2017) and $\log(g) = 4.6 \pm 0.1$ from the Gaia EDR3 catalog. The planet-to-star radius ratio (R_p/R_*) was allowed to vary during the fitting process. The transit depths computed by Iraclis are provided in Table A2.

From the posterior retrieval of Case I, we obtained a planetary temperature of 900^{+500}_{-400} K, consistent with previous studies by A. Tsiaras et al. (2018; 957.27 ± 343.3 K) and K. L. Chubb et al. (2020; $857.66^{+419.17}_{-288.89}$ K). The retrieved log water volume mixing ratio was $-0.5^{+0.3}_{-2.3}$, with a reduced chi-square of $\chi^2_{\rm red} = 1.70$. However, the posterior distribution exhibited two distinct solutions (see Figure E1). We therefore applied a k-means clustering algorithm to separate the results into two subcases.

In Case I.I, the derived temperature was 500^{+200}_{-100} K, consistent within 1σ of the value reported by L. Kreidberg et al. (2014; $639.5^{+144.6}_{-129.2}$ K). The retrieved log water abundance was -2^{+1}_{-2}, consistent within 1σ with B. Edwards et al. (2023), A. Tsiaras et al. (2016a), I. C. Weaver et al. (2020), K. L. Chubb et al. (2020), and D. Bartelt et al. (2025). In Case I.II, the temperature was 1200^{+300}_{-300} K, which agrees within 1σ with the study by D. Bartelt et al. (2025; $1013.17^{+147.45}_{-119.45}$ K)

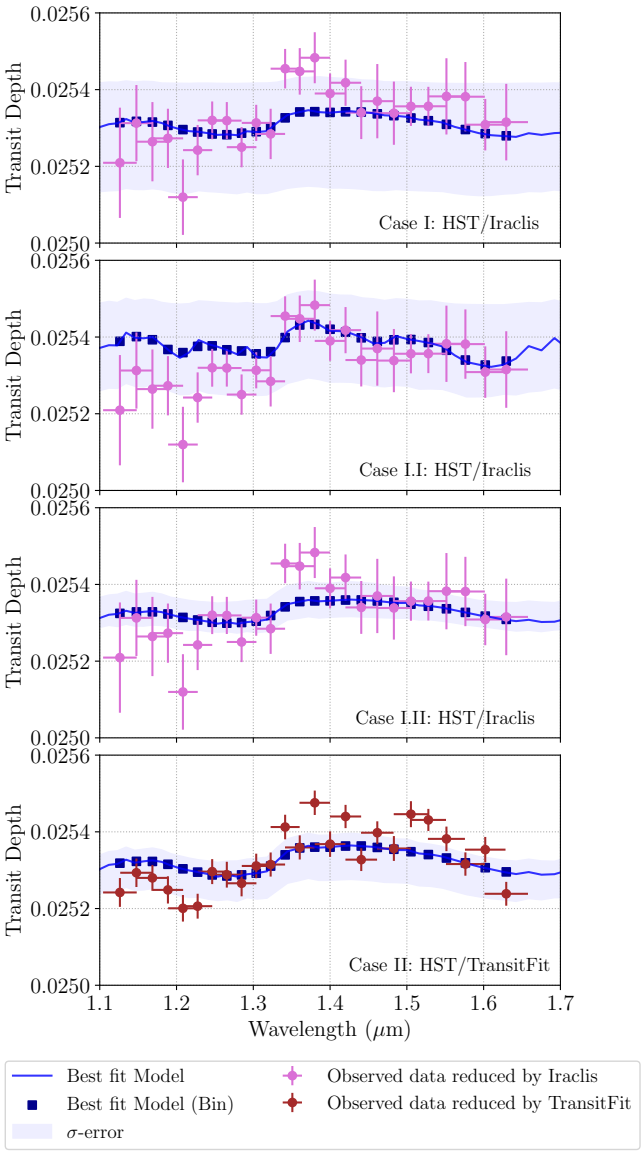

Figure 9. The best-fit transmission spectrum model of WASP-43 b derived from HST data. The synthetic model generated by `TauREx` is shown as a solid blue line, with the corresponding 1σ confidence region indicated by the blue shading. The binned best-fit model values are shown as blue squares. The transit depths computed with `Iraclis` and `TransitFit` are shown as pink and dark-red circles, respectively.

and A. Tsiaras et al. (2018). The retrieved log water abundance was $-0.4^{+0.2}_{-0.1}$ for Case I.II, consistent with the value found in the overall Case I retrieval. The $\chi^2_{\rm red}$ values for Case I.I and Case I.II were 1.95 and 1.39, respectively. The three retrievals of the HST/WFC3 G141 transmission spectrum reduced with `Iraclis` showed that no additional molecular species were detected at a significant level in any of the cases. The best-fit transmission spectrum for the HST data processed with `Iraclis` is displayed in Figure 9, and the resulting atmospheric parameters are listed in Table 7.

5.2. Case II: HST/WFC3 G141 Transmission Spectrum with `TransitFit`

For the HST/WFC3 G141 light curves fitted with `TransitFit`, the retrieved planetary temperature was 1200^{+200}_{-100} K, matching the result from Case I.II and consistent with A. Tsiaras et al. (2018) and D. Bartelt et al. (2025). The log water abundance was $-0.5^{+0.1}_{-0.1}$ with a $\chi^2_{\rm red} = 5.41$. While this value is notably higher than the $\chi^2_{\rm red}$ of 1.7 obtained in Case I, the difference is primarily driven by the transit depth errors from `TransitFit` being approximately half the size of those from `Iraclis`. This difference in error estimation is a result of the different sampling algorithms used, specifically nested sampling (`dynesty`) in `TransitFit` and MCMC (`emcee`) in `Iraclis`. Furthermore, variations in the detrending and limb-darkening methods also contribute to this discrepancy. Despite the different $\chi^2_{\rm red}$ values, the two fits are statistically consistent. Aside from the water feature discussed, no other molecular species were significantly detected.

The retrieval results are summarized in Table 7, with the best-fit spectrum shown in Figures E1 and 9. From the analysis of the HST/WFC3 G141 transmission spectra reduced with both `Iraclis` and `TransitFit`, the retrieved water abundances were consistently associated with the higher-temperature solutions, as seen in Case I, Case I.II, and the `TransitFit` retrieval (Case II).

5.3. Case III: Full Transmission Spectrum Using `Iraclis`-reduced HST Data

As with Case I and Case II, our initial analysis was limited to transmission spectra obtained from HST/WFC3 G141. To achieve a comprehensive statistical analysis of the atmospheric chemical composition of WASP-43 b, we expanded the dataset by combining the HST spectra with observations from ground-based facilities, TESS, and JWST. This extension broadens the wavelength coverage from the 1.1–1.6 μm range to 0.3–10 μm. Given that the HST transmission spectra in Case I and Case II were processed using different reduction tools, we maintained this distinction in the combined analysis, separating them into Case III and Case IV.

For the JWST/MIRI data, we utilized the spectroscopic light curves directly from T. J. Bell et al. (2024). We applied a second-order polynomial detrending model within `TransitFit` to independently determine the transit depth for each channel. Unlike the discrepancy observed in the HST data analysis, the resulting transmission spectrum derived via `TransitFit` for the JWST data is consistent with the values reported by T. J. Bell et al. (2024) using the `Eureka!` pipeline.

In total, we utilized 82 transmission spectra, excluding the Clear filter data listed in Table A1. We note that an instrumental offset was applied to the JWST/MIRI observations relative to the other datasets, with the magnitude of this offset determined via a weighted average of the combined data, as in D. Grant et al. (2023). Additionally, while the standard `PHOENIX` stellar models cover the spectral range from 50 nm to 5.5 μm, the JWST/MIRI spectrum extends from 5 to 12 μm. To address this, we extrapolated the `PHOENIX` model to fit the transmission spectra beyond 5.5 μm.

The best-fit transmission spectrum for Case III is shown in Figure 10, with the corresponding posterior distribution in Figure E2. Despite the inclusion of an instrumental offset for the JWST/MIRI spectrum, the combination of data over such a broad wavelength range introduced significant modeling complexities, resulting in high residuals that make the retrieval of reliable atmospheric parameters difficult. We find that in this regime the evidence for H_2O diminishes to nonsignificant levels, and no other molecular species are robustly detected.

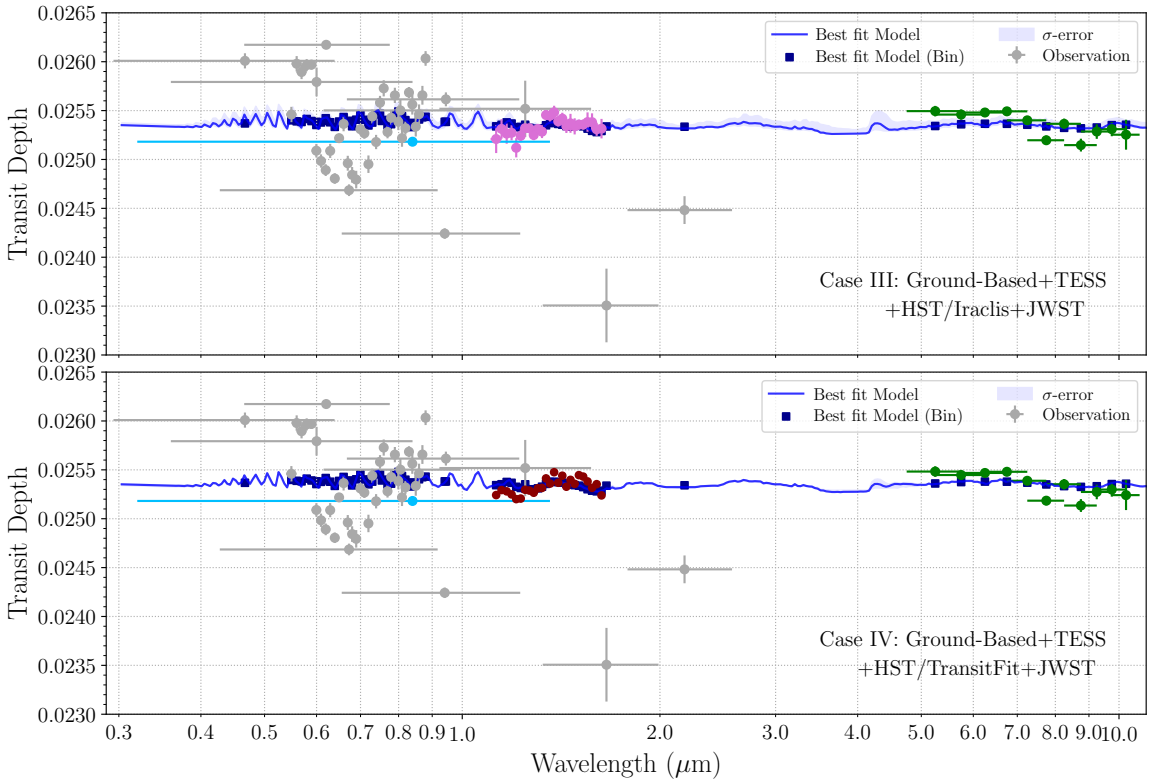

Figure 10. The best-fit transmission spectrum model of WASP-43 b, calculated for the combined dataset including ground-based observations (gray circles), TESS (light-blue circles), HST processed with `Iraclis` (pink circles), HST processed with `TransitFit` (dark-red circles), and JWST (green circles). The synthetic model generated by `TauREx` is shown as a solid blue line, with the corresponding 1σ confidence region indicated by the blue shading. The binned best-fit model values are shown as blue squares. Note that the five outlier transit depths in the optical wavelength range correspond to the *R*, *I*, z', *H*, and *K* filters, respectively.

5.4. Case IV: Full Transmission Spectrum Using `TransitFit`-reduced HST Data

We define Case IV by combining the HST/WFC3 G141 transmission spectra reduced with `TransitFit` (Case II) with the transmission spectra from ground-based observations, TESS, and JWST, which were also reduced with `TransitFit`. Similar to Case III, the increased complexity of the broad-baseline retrieval for Case IV limited our ability to achieve a statistically robust model fit. This confirms that when the full wavelength coverage is considered with current data, the water abundance is not detected at a significant level. High-precision data across these wavelengths remain essential to overcome these complexities and break existing model degeneracies.

6. Conclusions

In this study, we conducted ground-based multiband follow-up observations of the hot Jupiter WASP-43 b using the SPEARNET network. A total of 35 transit light curves were obtained and combined with data from HST, TESS, JWST, and 109 previously published ground-based light curves. These datasets were used to model the transit light curves and refine the planetary parameters of WASP-43 b using `TransitFit`.

A total of 188 midtransit times, measured with `TransitFit`, were analyzed to investigate potential timing variations in WASP-43 b. No strong evidence for orbital decay was found, with $dP_d/dE = -3^{+1}_{-1} \times 10^{-11}$ days per orbit. Additionally, periodogram analysis also showed no significant TTVs. While F. Davoudi et al. (2021) reported a downward trend in TESS data from Sectors 09 and 35, our analysis of timing residuals ($O - C$) from four TESS sectors, including the latest Sector 89, showed no variability over a 7 yr interval. Moreover, simulations using `TTVFaster` further suggest that no planet with a mass greater than $10^2\ M_\oplus$ could exist with an orbital period of less than 2 days.

The atmospheric retrieval analysis of WASP-43 b reveals a distinct dependency of the retrieved parameters on wavelength coverage and data reduction methodology. The HST-only retrievals with both `Iraclis` (Case I) and `TransitFit` (Case II) indicate planetary temperatures ranging from 500 to 1200 K with higher water abundances, aligning with previous studies. However, the combined broader optical-to-mid-infrared baseline from SPEARNET, TESS, and JWST (Case III and Case IV) presents significant modeling challenges that limit the reliability of atmospheric characterization. In these two specific cases, the integration of data across such an extensive wavelength range introduced substantial complexities, making it difficult to achieve a statistically robust model fit. Therefore, high-precision transmission spectroscopy spanning a broad wavelength range is essential to overcome these modeling complexities and achieve a more reliable atmospheric characterization.

Acknowledgments

We thank the referee for the helpful and constructive comments that have improved this work. The observation data used in this work are based on observations made with ULTRASPEC at the Thai National Observatory, the Thai Robotic Telescopes, and the Regional Observatories for the

Public under the operation of the National Astronomical Research Institute of Thailand (Public Organization). The simulation section in this work was performed using the CHALAWAN NARIT High-Performance Computing (CHALAWAN HPC) system.

This work used the available data based on observations made with the NASA/ESA Hubble Space Telescope (HST) obtained from the Space Telescope Science Institute (STScI), which is operated by the Association of Universities for Research in Astronomy (AURA), Inc., under NASA contract NAS 5-26555. The published HST data present here were taken as part of proposal 13467, led by Jacob Bean. This paper also includes data collected with the TESS mission, obtained from the MAST data archive at the STScI. Funding for the TESS mission is provided by the NASA Explorer Program. STScI is operated by AURA, Inc., under NASA contract NAS 5-26555. The specific observations analyzed were obtained from the Hubble Source Catalog (STScI 2016) and the "TESS Light Curves—All Sectors" (TESS Team 2021) repositories. This work also used the data based on observations made with the NASA/ESA/CSA James Webb Space Telescope. The data were obtained from the MAST at the STScI, which is operated by AURA, Inc., under NASA contract NAS 5-03127 for JWST. These observations are associated with program proposal JWST-ERS-1366, led by Taylor J. Bell. This research made use of the open-source Python package `ExoCTK`, the Exoplanet Characterization Toolkit (M. Bourque et al. 2021).

We thank Zoltán Garai for providing the observational data from MuSCAT2 and Quentin Changeat for suggesting the instructions on TauREx. This work is supported by the Fundamental Fund of Thailand Science Research and Innovation (TSRI) through the National Astronomical Research Institute of Thailand (Public Organization; FFB690072/0269).

Facilities: HST, TESS, JWST, 2.4-m (TNT), 1-m (TNT), TRT, 0.7-m (ROP-NM) and 0.7-m (ROP-CC).

Software: `Sextractor` (E. Bertin & S. Arnouts 1996), `Astrometry.net` (D. Lang et al. 2010), `TransitFit` (J. J. C. Hayes et al. 2024), `TTVFaster` (K. M. Deck & E. Agol 2016), `Iraclis` (A. Tsiaras et al. 2016a), and `TauREx` (A. F. Al-Refaie et al. 2021).

Appendix A
The Planet Radius and Limb Darkening

The planet-to-star radius ratios and quadratic limb-darkening coefficients derived from TransitFit and Iraclis are presented in Tables A1 and A2, respectively.

Table A1
The Planet-to-star Radius Ratio (R_p/R_*), Transit Depth, and Quadratic LDCs of WASP-43 b in 83 Different Filters, as Obtained by `TransitFit`

Filter	Midwavelength (μm)	Bandwidth (μm)	R_p/R_*	Transit Depth (%)	u_0	u_1
$I + z'$ band	0.944	0.27	0.1600 ± 0.0002	2.562 ± 0.007	0.34 ± 0.01	0.33 ± 0.03
r' band	0.621	0.16	0.1618 ± 0.0001	2.617 ± 0.004	0.570 ± 0.009	0.455 ± 0.008
g' band	0.467	0.17	0.1613 ± 0.0002	2.601 ± 0.008	0.67 ± 0.02	0.56 ± 0.02
...	...	...	...	...	...	...
...	...	...	...	...	...	...

(This table is available in its entirety in machine-readable form in the online article.)

Table A2
The Planet-to-star Radius Ratio (R_p/R_*) and Transit Depths of WASP-43 b Derived by `Iraclis`

Filter	Midwavelength (μm)	Bandwidth (μm)	R_p/R_*	Transit Depth (%)
HST/WFC3 G141	1.126	0.022	0.1588 ±0.0005	2.52 ± 0.01
HST/WFC3 G141	1.148	0.021	0.1591 ±0.0003	2.53 ± 0.01
HST/WFC3 G141	1.169	0.021	0.1589 ±0.0003	2.53 ± 0.01
...	...	...	...	...
...	...	...	...	...

(This table is available in its entirety in machine-readable form in the online article.)

Appendix B
WASP-43 b's Midtransit Times and Timing Residuals

The midtransit times (t_0) and timing residuals ($O - C$) for all 188 analyzed epochs are cataloged in Table B1.

Table B1
Midtransit Times (t_0) and Timing Residuals ($O - C$) for WASP-43 b from 188 Epochs or Transit Events

Epoch	$t_0 + 2400000$ (BJD_{TDB})	($O - C$) (days)	References
−2318	55537.81672 ± 0.00017	−0.00017	(a)
−2307	55546.76491 ± 0.00009	−0.00020	(a)
−2302	55550.83219 ± 0.00006	−0.00029	(a)
…	…	…	…
…	…	…	…

Note. The full table is available in a machine-readable format in the online journal. Data Source: (a) M. Gillon et al. (2012); (b) G. Chen et al. (2014); (c) G. Maciejewski et al. (2013); (d) F. Murgas et al. (2014); (e) HST; (f) D. Ricci et al. (2015); (g) I.-G. Jiang et al. (2016); (h) this study; (i) H. Parviainen et al. (2019); (j) Z. Garai et al. (2021b); (k) TESS; (l) JWST.

(This table is available in its entirety in machine-readable form in the online article.)

Appendix C
The Individual Transit Light Curves from SPEARNET Observations, HST, and TESS Modeled by `TransitFit` Fitting

The individual transit light curves from SPEARNET, HST, and TESS observations, modeled via TransitFit, are displayed in Figures C1, C2, and C3, respectively.

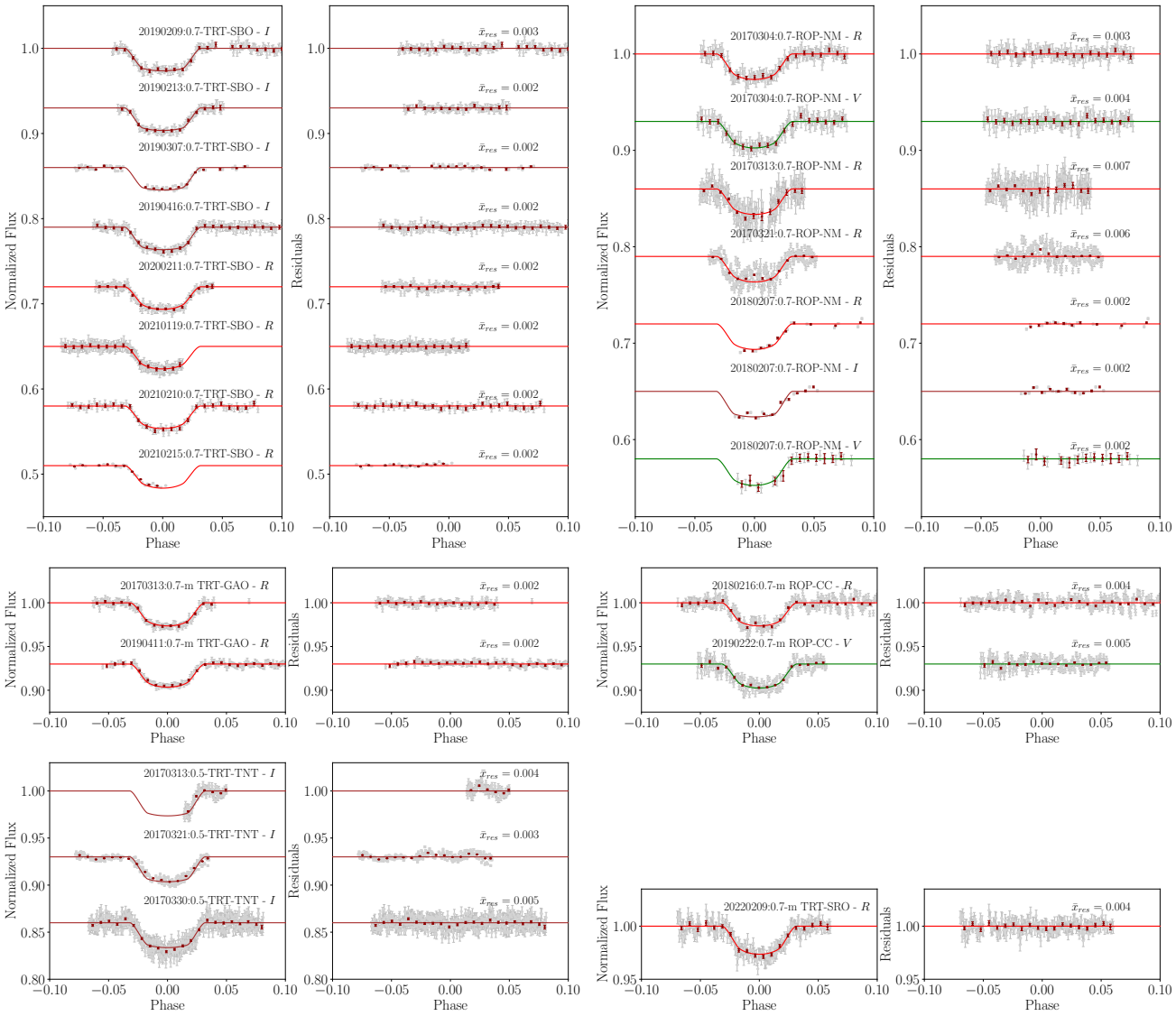

Figure C1. The individual SPEARNET transit light curves of WASP-43 b observed at TRT-SBO, ROP-NM, TRT-GAO, ROP-CC, TRT-TNT, and TRT-SRO. The observed data are shown as gray circles, with filters *R* (red), *I* (brown), and *V* (green). The corresponding residuals and the mean residual values ($\bar{x}_{\rm res}$) with clear offsets are displayed in the right panels.

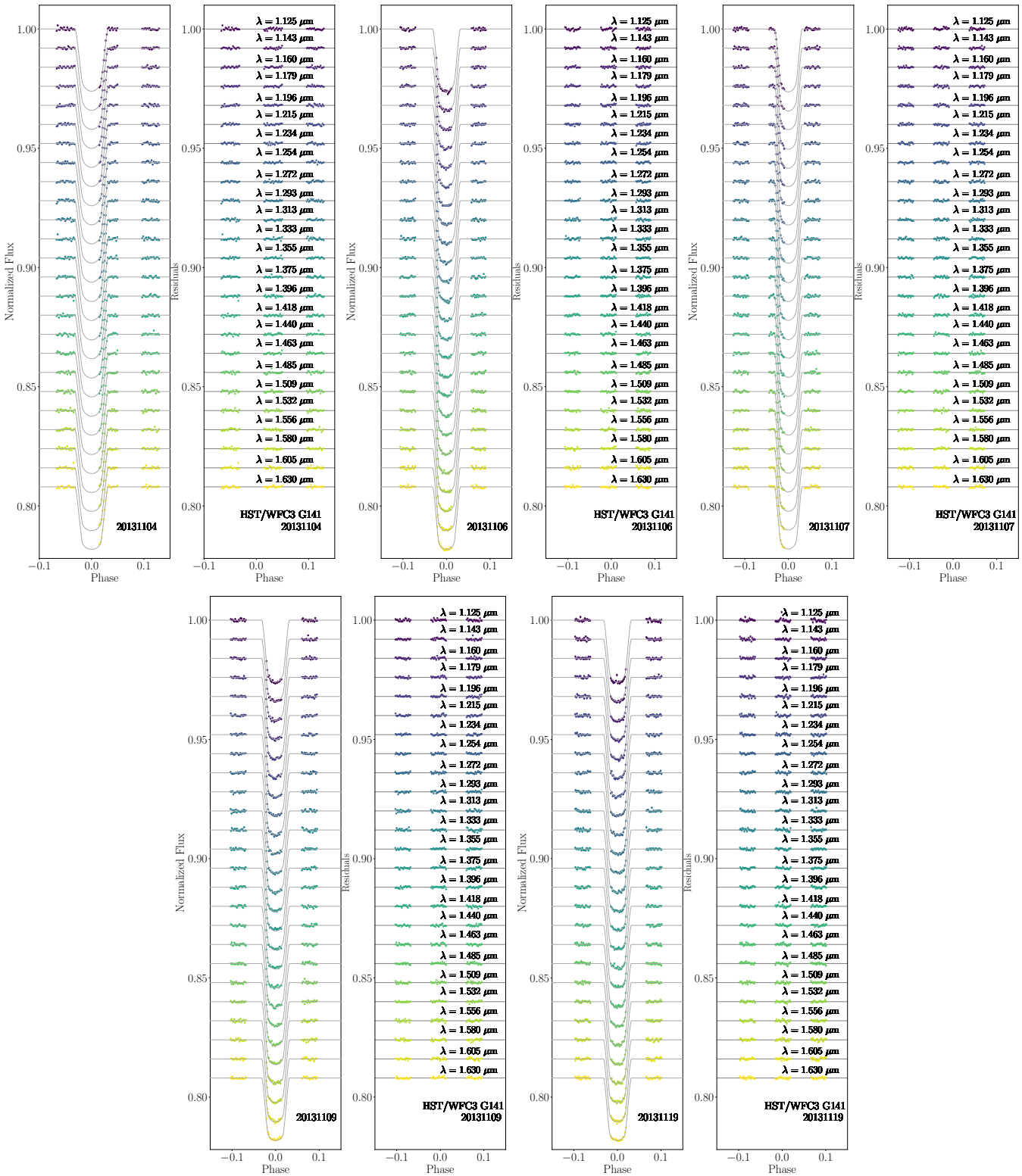

Figure C2. The HST transit light curves of WASP-43 b from the observations conducted between 2013 November 04 and 19. The observed data are represented as circles, and the `TransitFit` models are shown as solid lines. The corresponding residuals with clear offset are displayed in the right panels.

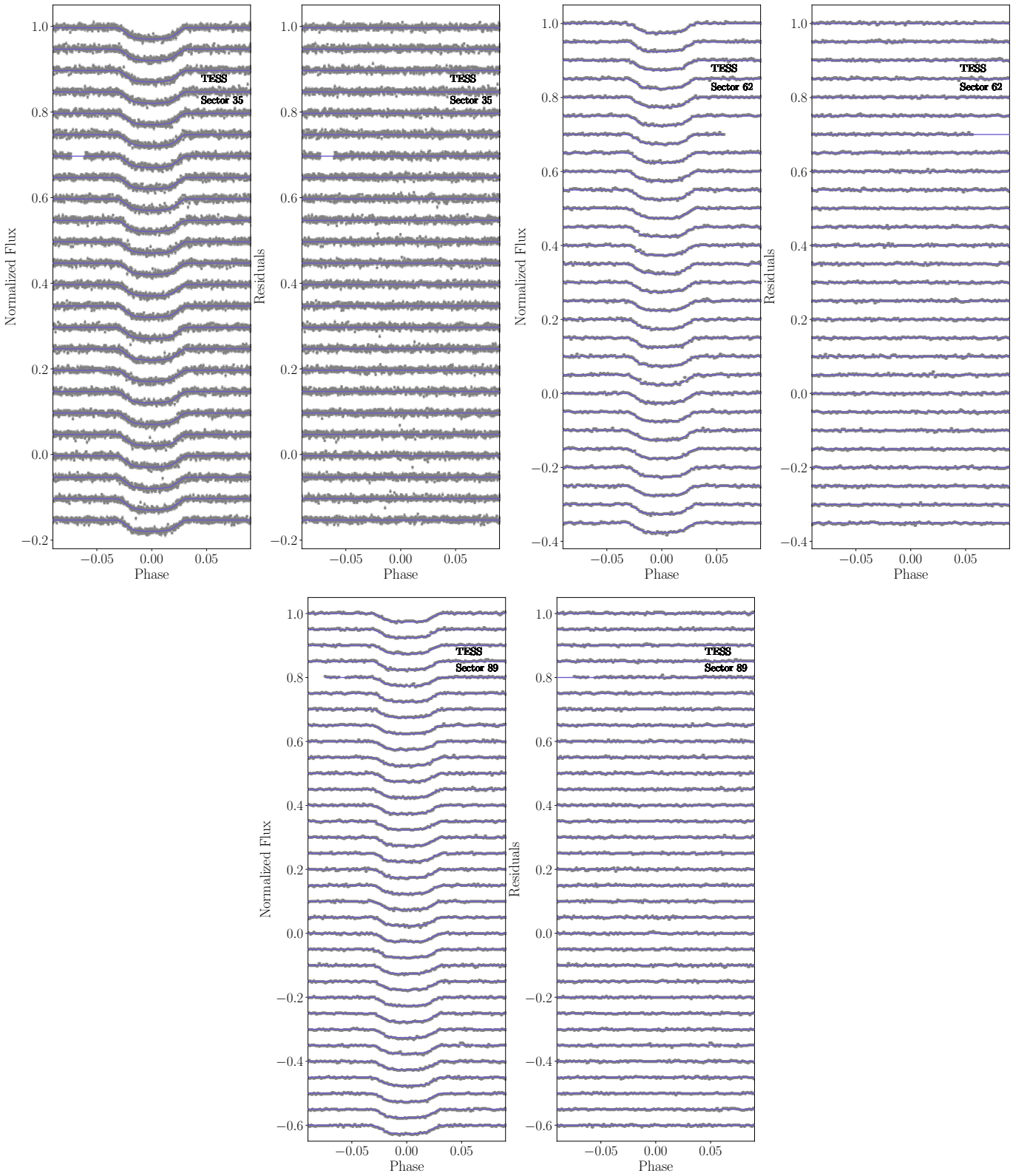

Figure C3. The TESS transit light curves of WASP-43 b from the observations in Sector 35, 62, and 89, respectively. The observed data are represented as circles, and the `TransitFit` models are shown as solid lines. The corresponding residuals with clear offset are displayed in the right panel.

Appendix D
Posterior Probability Distribution of the MCMC Fitting Parameters for Constant-period and Orbital Decay Models

The posterior probability distributions for the MCMC fitting parameters of the constant-period and orbital decay models are shown in Figure D1.

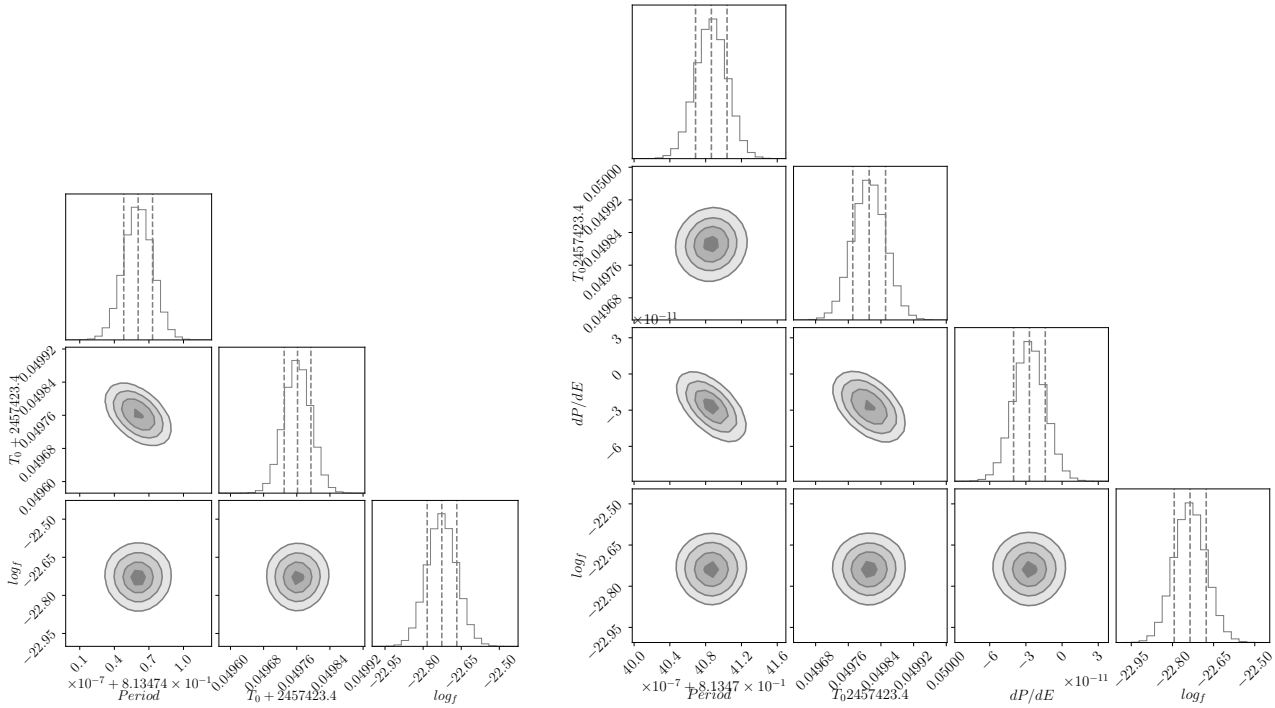

Figure D1. Posterior probability distribution of the MCMC fitting parameters for the constant-period model (left) and the orbital decay model (right).

Appendix E
Posterior Probability Distribution of the Transmission Spectrum Model for WASP-43 b, Using the `TauREx` Package with Nested Sampling

The posterior probability distributions for the transmission spectrum models using both the HST-only data and the full wavelength coverage generated via TauREx are illustrated in Figures E1 and E2, respectively.

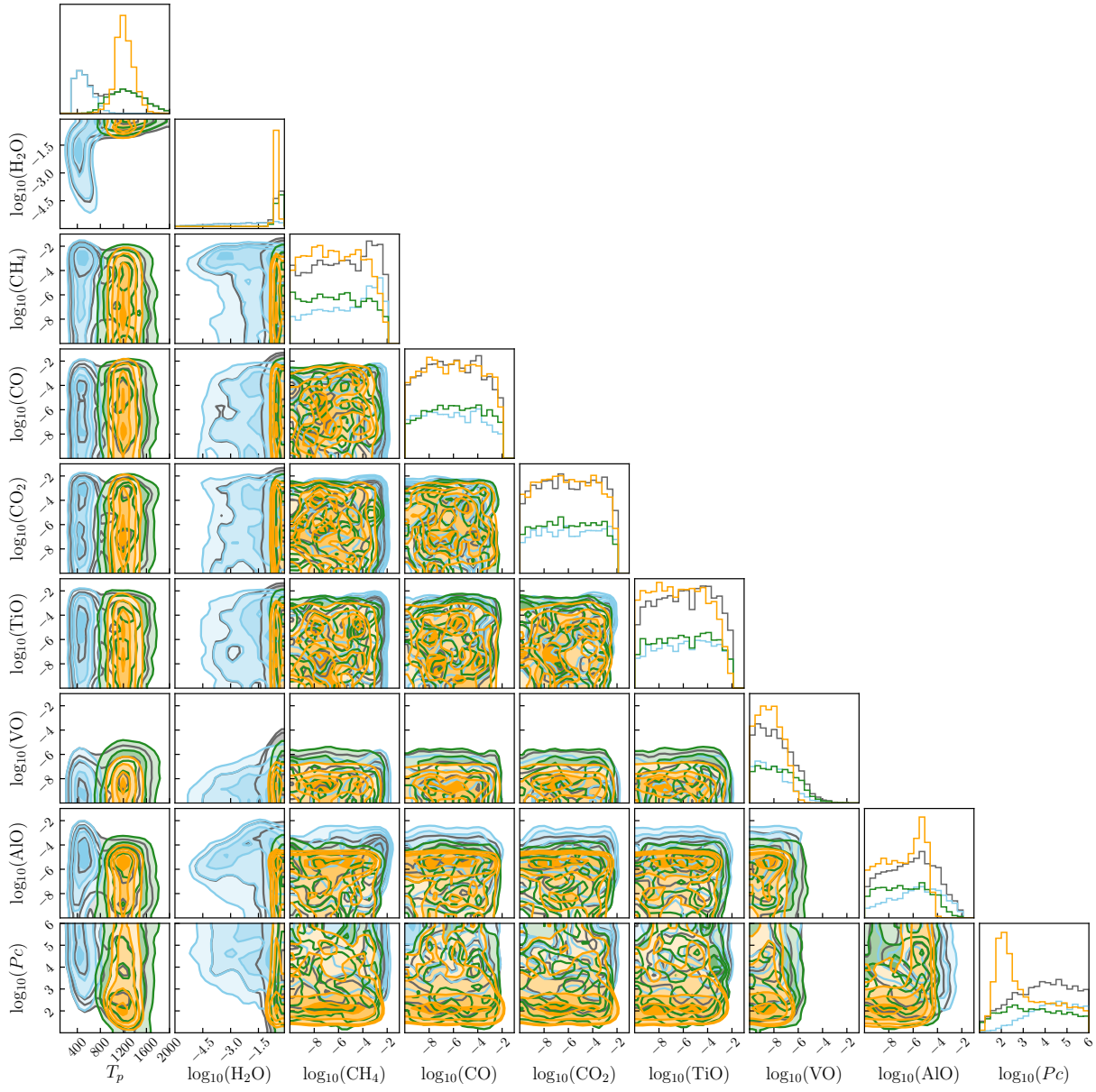

Figure E1. Posterior probability distributions for the transmission spectrum model of WASP-43 b using only HST data: Case I (gray), Case I.I (blue), and Case I.II (green) correspond to the HST/`Iraclis` reductions, while Case II (orange) corresponds to the HST/`TransitFit` reduction. The retrieved parameter values correspond to the 16th and 84th percentiles of the posterior distributions, representing the 1σ credible intervals.

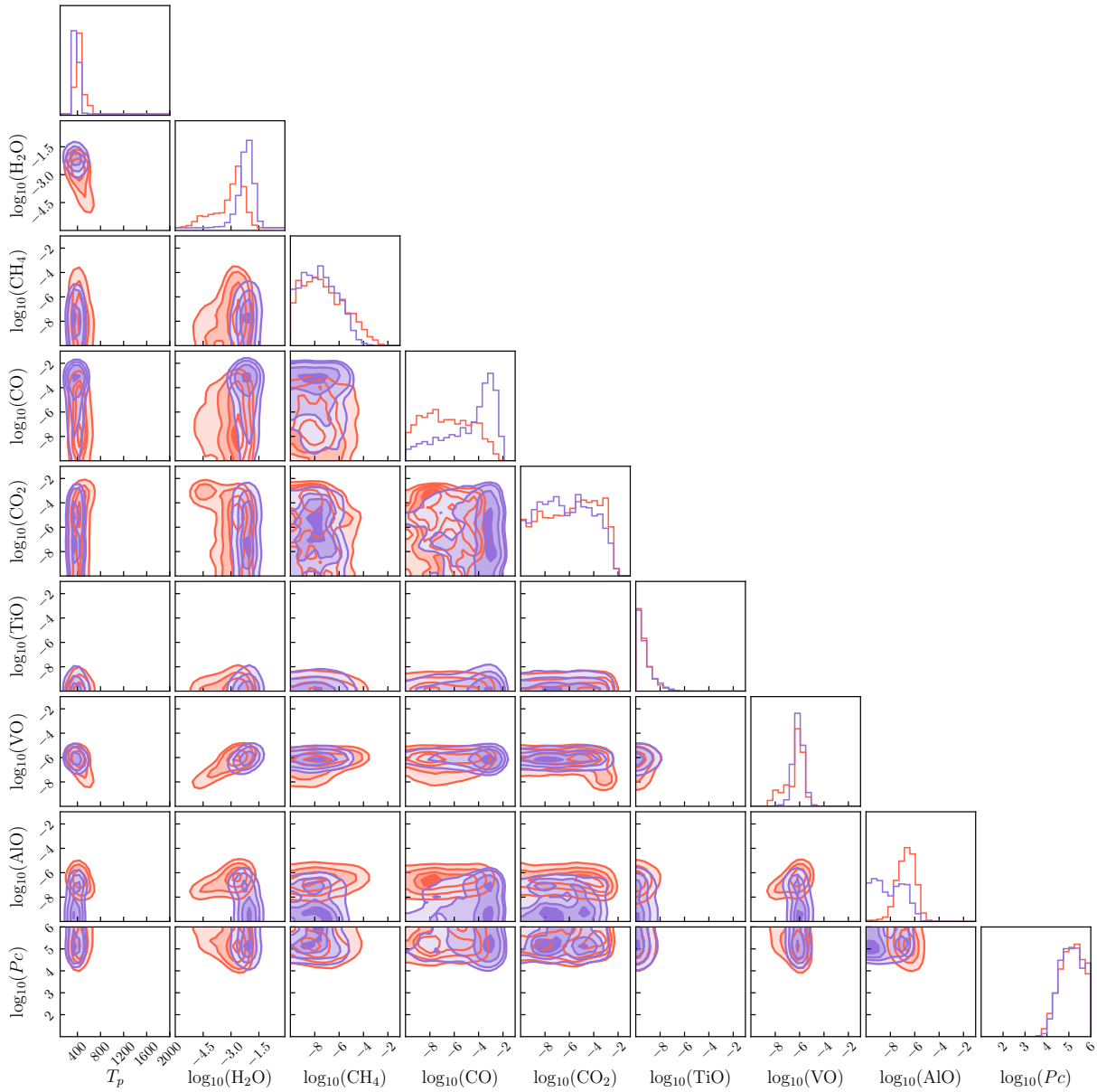

Figure E2. Posterior probability distributions for the transmission spectrum model of WASP-43 b across the full wavelength coverage: Case III, ground-based +TESS+HST/`Iraclis`+JWST (red); case IV, ground-based+TESS+HST/`TransitFit`+JWST (purple). The retrieved parameter values correspond to the 16th and 84th percentiles of the posterior distributions, representing the 1σ credible intervals.

ORCID iDs

Napaporn A-thano https://orcid.org/0000-0001-7234-7167
Supachai Awiphan https://orcid.org/0000-0003-3251-3583
Eamonn Kerins https://orcid.org/0000-0002-1743-4468
Akshay Priyadarshi https://orcid.org/0000-0003-1143-0877
Iain McDonald https://orcid.org/0000-0003-0356-0655
Ing-Guey Jiang https://orcid.org/0000-0001-7359-3300
Yogesh C. Joshi https://orcid.org/0000-0001-8657-1573
Fan Yang https://orcid.org/0000-0002-6039-8212
Patcharawee Munsaket https://orcid.org/0009-0000-3885-4229
Yasir Abdul Qadir https://orcid.org/0000-0001-5162-4225
Vik S Dhillon https://orcid.org/0000-0003-4236-9642

References

A-thano, N., Jiang, I.-G., Awiphan, S., et al. 2022, AJ, 163, 77
Abel, M., Frommhold, L., Li, X., & Hunt, K. L. C. 2011, JPCA, 115, 6805
Abel, M., Frommhold, L., Li, X., & Hunt, K. L. C. 2012, JChPh, 136, 044319
Al-Refaie, A. F., Changeat, Q., Waldmann, I. P., & Tinetti, G. 2021, ApJ, 917, 37
Awiphan, S., Kerins, E., Pichadee, S., et al. 2016, MNRAS, 463, 2574
Bartelt, D., Mansfield, M. W., Line, M. R., et al. 2025, AJ, 169, 101
Bell, T., Ahrer, E.-M., Brande, J., et al. 2022, JOSS, 7, 4503
Bell, T. J., Crouzet, N., Cubillos, P. E., et al. 2024, NatAs,
Bell, T. J., Kreidberg, L., Kendrew, S., et al. 2023, arXiv:2301.06350
Bertin, E., & Arnouts, S. 1996, A&AS, 117, 393
Blecic, J., Harrington, J., Madhusudhan, N., et al. 2014, ApJ, 781, 116
Bonomo, A. S., Desidera, S., Benatti, S., et al. 2017, A&A, 602, A107
Bourque, M., Espinoza, N., & Filippazzo, J. 2021, The Exoplanet Characterization Toolkit (ExoCTK), v1.0.0, Zenodo, doi:10.5281/zenodo.4556063
Chen, G., van Boekel, R., Wang, H., et al. 2014, A&A, 563, A40
Chubb, K. L., Min, M., Kawashima, Y., Helling, C., & Waldmann, I. 2020, A&A, 639, A3
Chubb, K. L., Rocchetto, M., Yurchenko, S. N., et al. 2021, A&A, 646, A21
Claret, A. 2000, A&A, 363, 1081
Czesla, S., Schröter, S., & Schneider, C. P. 2019, PyA: Python astronomy-related packages, Astrophysics Source Code Library, ascl:1906.010

Davoudi, F., Baştürk, Ö., Yalçínkaya, S., Esmer, E. M., & Safari, H. 2021, AJ, 162, 210
Deck, K. M., & Agol, E. 2016, ApJ, 821, 96
Dhillon, V. S., Marsh, T. R., Atkinson, D. C., et al. 2014, MNRAS, 444, 4009
Edwards, B., Changeat, Q., Tsiaras, A., et al. 2023, ApJS, 269, 31
Esposito, M., Covino, E., Desidera, S., et al. 2017, A&A, 601, A53
Fabrycky, D. C., Ford, E. B., Steffen, J. H., et al. 2012, ApJ, 750, 114
Feroz, F., Hobson, M. P., & Bridges, M. 2009, MNRAS, 398, 1601
Fletcher, L. N., Gustafsson, M., & Orton, G. S. 2018, ApJS, 235, 24
Foreman-Mackey, D., Hogg, D. W., Lang, D., & Goodman, J. 2013, PASP, 125, 306
Fulton, B. J., Shporer, A., Winn, J. N., et al. 2011, AJ, 142, 84
Garai, Z., Pribulla, T., Parviainen, H., et al. 2021a, MNRAS, 508, 5514
Garai, Z., Pribulla, T., Parviainen, H., et al. 2021b, MNRAS, 508, 5514
Gillon, M., Triaud, A. H. M. J., Fortney, J. J., et al. 2012, A&A, 542, A4
Gordon, I., Rothman, L. S., Wilzewski, J. S., et al. 2016, AAS Meeting , 48, 421.13
Grant, D., Lewis, N. K., Wakeford, H. R., et al. 2023, ApJL, 956, L32
Hayes, J. J. C., Priyadarshi, A., Kerins, E., et al. 2024, MNRAS, 527, 4936
Hellier, C., Anderson, D. R., Collier Cameron, A., et al. 2011, A&A, 535, L7
Hoyer, S., Pallé, E., Dragomir, D., & Murgas, F. 2016, AJ, 151, 137
Husser, T. O., Wende-von Berg, S., Dreizler, S., et al. 2013, A&A, 553, A6
Ivshina, E. S., & Winn, J. N. 2022, ApJS, 259, 62
Jenkins, J. M., Twicken, J. D., McCauliff, S., et al. 2016, SPIE, 9913, 99133E
Jiang, I.-G., Lai, C.-Y., Savushkin, A., et al. 2016, AJ, 151, 17
Kanodia, S., & Wright, J. 2018, RNAA, 2, 4
Kokori, A., Tsiaras, A., Edwards, B., et al. 2023, ApJS, 265, 4
Kreidberg, L. 2015, PASP, 127, 1161
Kreidberg, L., Bean, J. L., Désert, J.-M., et al. 2014, ApJL, 793, L27
Kreidberg, L., Line, M. R., Thorngren, D., Morley, C. V., & Stevenson, K. B. 2018, ApJL, 858, L6
Lang, D., Hogg, D. W., Mierle, K., Blanton, M., & Roweis, S. 2010, AJ, 139, 1782
Lesjak, F., Nortmann, L., Yan, F., et al. 2023, A&A, 678, A23
Maciejewski, G., Puchalski, D., Saral, G., et al. 2013, IBVS, 6082, 1
McDonald, I., van Loon, J. T., Decin, L., et al. 2009, MNRAS, 394, 831
McDonald, I., Zijlstra, A. A., & Boyer, M. L. 2012, MNRAS, 427, 343
McDonald, I., Zijlstra, A. A., & Watson, R. A. 2017, MNRAS, 471, 770
McKemmish, L. K., Masseron, T., Hoeijmakers, H. J., et al. 2019, MNRAS, 488, 2836
McKemmish, L. K., Yurchenko, S. N., & Tennyson, J. 2016, MNRAS, 463, 771
Murgas, F., Pallé, E., Zapatero Osorio, M. R., et al. 2014, A&A, 563, A41
Parviainen, H., Tingley, B., Deeg, H. J., et al. 2019, A&A, 630, A89
Patra, K. C., Winn, J. N., Holman, M. J., et al. 2020, AJ, 159, 150
Patrascu, A. T., Hill, C., Tennyson, J., & Yurchenko, S. N. 2014, JChPh, 141, 144312
Polyansky, O. L., Kyuberis, A. A., Zobov, N. F., et al. 2018, MNRAS, 480, 2597
Ricci, D., Ramón-Fox, F. G., Ayala-Loera, C., et al. 2015, PASP, 127, 143
Rothman, L. S., & Gordon, I. E. 2014, in in 13th Int. HITRAN Conf., 49
Speagle, J. S. 2020, MNRAS, 493, 3132
Stevenson, K. B., Line, M. R., Bean, J. L., et al. 2017, AJ, 153, 68
STScI 2016, Hubble Source Catalog, MAST, doi:10.17909/T97P46
Tennyson, J., Yurchenko, S. N., Al-Refaie, A. F., et al. 2016, JMoSp, 327, 73
TESS Team 2021, TESS Light Curves - All Sectors, MAST, doi:10.17909/T9-NMC8-F686
Tody, D. 1986, SPIE, Vol. 627, 733
Tody, D. 1993, ASPC, 52, 173
Tody, D. 2016, pylightcurve: Exoplanet lightcurve model, Astrophysics Source Code Library, ascl:1612.018
Tsiaras, A., Rocchetto, M., Waldmann, I. P., et al. 2016a, ApJ, 820, 99
Tsiaras, A., Waldmann, I. P., Rocchetto, M., et al. 2016b, ApJ, 832, 202
Tsiaras, A., Waldmann, I. P., Zingales, T., et al. 2018, AJ, 155, 156
Weaver, I. C., López-Morales, M., Espinoza, N., et al. 2020, AJ, 159, 13
Wong, I., Shporer, A., Daylan, T., et al. 2020, AJ, 160, 155
Yurchenko, S. N., Mellor, T. M., Freedman, R. S., & Tennyson, J. 2020, MNRAS, 496, 5282
Yurchenko, S. N., Owens, A., Kefala, K., & Tennyson, J. 2024, MNRAS, 528, 3719
Zechmeister, M., & Kürster, M. 2009, A&A, 496, 577